THE DEVELOPMENT OF MICRO-GAS CHROMATOGRAPHY SYSTEM WITH INTEGRATED PHOTONIC CRYSTAL SENSORS

by

PRIYANKA BISWAS

Presented to the Faculty of the Graduate School of

The University of Texas at Arlington in Partial Fulfillment

of the Requirements

for the Degree of

DOCTOR OF PHILOSOPHY

THE UNIVERSITY OF TEXAS AT ARLINGTON

August 2021

Doctoral Committee:

Professor Yuze (Alice) Sun, Chair
Professor Sungyong Jung
Professor Qilian Liang
Professor Chenyun Pan
Professor Weidong Zhou

Priyanka Biswas

priyanka.biswas@mavs.uta.edu

Acknowledgements

I would like to thank the following people who have helped me on my research: my supervisor Dr. Yuze (Alice) Sun, for her passion on the projects, for her support, guidance, and patience; the Shimazu Institute Nano Technology Research Center, Shimadzu Center for Advanced Analytical Chemistry and University of Texas at Arlington, for providing the facility for the fabrication and testing of my devices. I also thank all my friends that have helped me to get through the hardships during my PhD program. Thanks to my family members for their encouragement and unconditional support.

07. 14. 2021

Abstract

THE DEVELOPMENT OF MICRO-GAS CHROMATOGRAPHY SYSTEM WITH INTEGRATED PHOTONIC CRYSTAL SENSORS

PRIYANKA BISWAS, PhD

The University of Texas at Arlington, 2021

Supervising Professor: Yuze Sun

Miniaturization of gas chromatography (GC) systems have made it possible to utilize the analytical technique in on-site applications without having to compromise data reliability offered by the conventional benchtop GC. Various types of miniaturized microsensors and nanosensors have been developed for a micro-gas chromatography (μGC) system. However, integration of an appropriate detector in μGC systems still face significant challenge. We present a solution to the problem through integration of μGC with photonic crystal slab (PCS) sensors using transfer printing technology. This integration offers an opportunity to utilize the advantages of optical sensors such as high sensitivity, immunity to electromagnetic interference, rapid response time and at the same time compensates for the lack of detection specificity which label-free optical sensors suffer from. We transfer printed a 2D defect free PCS on a borofloat glass, bonded it to a silicon microfluidic gas cell or directly to a microfabricated GC column and then coated it with a gas responsive polymer. Realtime spectral shift in Fano resonance of the PCS sensor was used to quantitatively detect analytes over a mass range of 3 orders. The

integrated μGC-PCS system was used to demonstrate separation and detection of a complex mixture of 10 chemicals consisting of alkanes, benzene derivatives, ketone, aldehyde, and alkene derivative. Fast separation and detection (4.2 min) and a low detection limit (~ ng) was demonstrated for all the analytes.

Table of Contents

List of Illustrations

List of Tables

Chapter 1

Introduction

1.1 Micro-Gas Chromatography

Gas Chromatography is a quintessential analytical method to separate and analyze complex mixtures of volatile organic compounds used in industry and academia. Although the name suggests that it is applicable to samples in gas phase, but actually liquid and solid samples have also been analyzed using gas chromatography after going through some form of chemical preprocess. Figure 1-1 shows a generic gas chromatography system composed of sample injection unit, column, and detector [1]. The sample injection system collects the sample and delivers it to the column where the analytes get separated. It utilizes a physical method of separation based on partition of the gas molecules between a mobile phase and a stationary phase. At the end of the column the analytes pass through a detector producing a readable signal.

Although benchtop GC systems have been evaluating complex gaseous sample with high precision and reliability the requirement to use it in a gamut of environments and high cost involved in procurement and maintenance called for miniaturization. Figure 1-2 shows a benchtop GC and a micro gas chromatography (μGC) [2]. The pioneering initiative to miniaturize this technology was taken by Stephen C. Terry in 1979 [3]. Conventional microfabrication techniques were used to develop a sample injection system, separation column and thermal conductivity detector on silicon substrate. The system showed moderate separation performance and poor detection limit with very short analysis time. Since then, μGC has come a long way in terms of fabrication procedures, performance, size, and application.

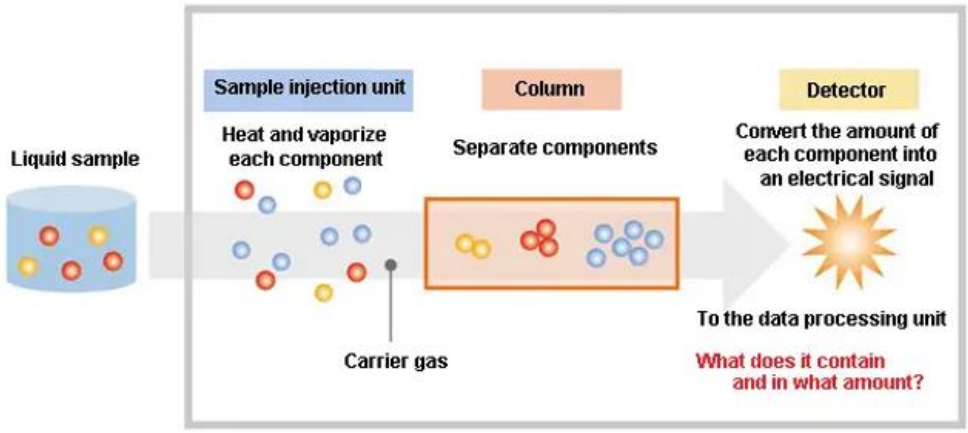

Figure 1-1 Schematic outlining the operation of gas chromatography [1]

The increasing need for analyzing and identifying chemicals in environmental, defense, health and beauty applications have led to the popularity of µGC systems. According to recent trends, unlike what its name suggests, these group of instrument includes all portable gas chromatography system irrespective of its fabrication technique or weight. The key features of such a system are compact, automatic, reduced power consumption, minimal production, and maintenance costs and suitable for field analysis. Thus, it provides the advantages of rapid analysis and turnaround time as well as simpler sample preparation and introduction mechanism reducing the probability of modifying the original sample. Over the last decade researchers have invested their efforts in making these systems more efficient and suitable for mass use.

(a) (b)

Figure 1-2 An example of (a) benchtop Commercial GC system (Agilent 8860) (b) µGC system [2]

1.2 Photonic Crystal

Photonic crystals (PC) are defined as periodic structures of different dielectric material with the goal of manipulating the propagation of light through it. The high and low dielectric periodicity can exploit the movement of photons similar to the motion of electrons controlled by periodic potential of semiconductor by establishing allowed and forbidden energy bands [4, 5]. Consequentially there is no transmission of light in certain range of frequencies called the photonic band gap (PBG). For some optical applications different kinds of defects are introduced in the structure. The defect causes localized photonic states in the PBG whose shape and properties are determined by the defect type. This breaks the periodicity and localizes light in the PBG region allowing for control and manipulation of the light. A line defect could behave like a waveguide, point defect like a micro cavity and planar defect could imitate a perfect mirror.

Depending on the dimension of periodicity photonic crystals can be classified into 1D, 2D and 3D as shown in Figure 1-3 [6]. 1D PC has periodic modulation of different dielectric material in a single direction only. This results in the PBG to exist in

the direction of periodicity for any refractive index contrast. Width of the PBG depends on the refractive index contrast in this case. 1D PCs have application in high efficiency mirrors, optical filters, waveguides and lasers along with antireflection coatings on optical components like lenses and prisms [7-13]. Periodicity in two different directions with uniform refractive index in the third direction result in 2D PCs. When the lattice has high refractive index contrast, PBG arise in the plane of periodicity perpendicular to the rod axis as shown in Figure 1-3(b). Higher dielectric rods in lower dielectric air lattice provides PBG for the transverse magnetic (TM) mode where the E field is polarized perpendicular to the plane of periodicity. Likewise lower dielectric air holes in a higher dielectric host give PBG for the transverse electric modes where H field is polarized perpendicular to the plane of periodicity. 3D PCs have periodicity modulation in all three directions. Given the structure has large enough refractive index contrast and favorable periodicity, a PBG occurs in all directions. This allows them to reflect light incident from any direction. Among the three, researchers are more interested in 2D PCs due to its valuable optical properties and ease of fabrication using standard clean room protocols.

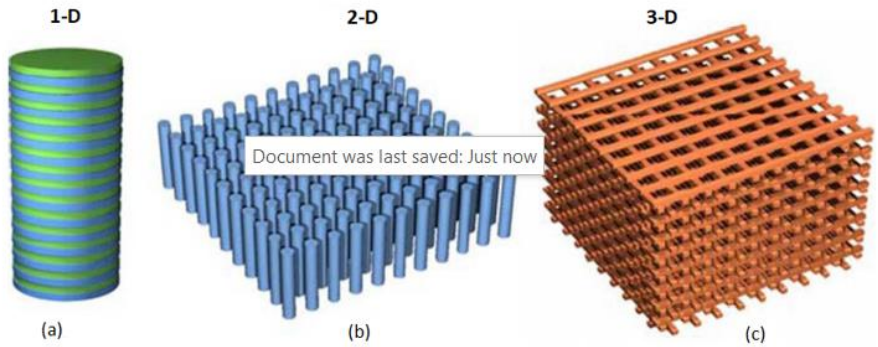

Figure 1-3 Schematic illustration of (a)1D (b) 2D (c) 3D photonic crystals [6]

1.3 Motivation

Optical detection methods are extensively popular in chemical and biological sensing. The rapid rise in application fields is shifting even more attention towards it in recent time. This method of detection offers advantages like remote sensing, immunity to electromagnetic interference and sensor multiplexing on a single chip. Typically, optical sensing can be divided in two broad classes-label free, and label based. Figure 1-4 shows the general principle between the two [14]. Label based sensing requires a fluorescent or radioactive tag attached to either the target or the receptor molecule. Radiation intensity of the tag molecule would represent the presence of the target molecule or the bonding strength between the target and the receptor. Although this technique is highly sensitive and have shown potential in commercial scope there are still some drawbacks. The process of attaching the labels is often an arduous task and may modify the functionality of the target molecule making it unsuitable for in vivo application. Also, some knowledge regarding the presence of the target molecule is required beforehand for successful detection. Variation in fluorescence efficiency and unpredictability in target and receptor kinetics makes quantitative analysis hard. On the other hand, for label free sensing, target molecule labeling is not required and the physical properties of the target molecule such as mass, permittivity, phase, polarization or conductivity is measured via interaction with light. Hence the technique is less aggressive on the target/ receptor molecules and do not affect their functionality.

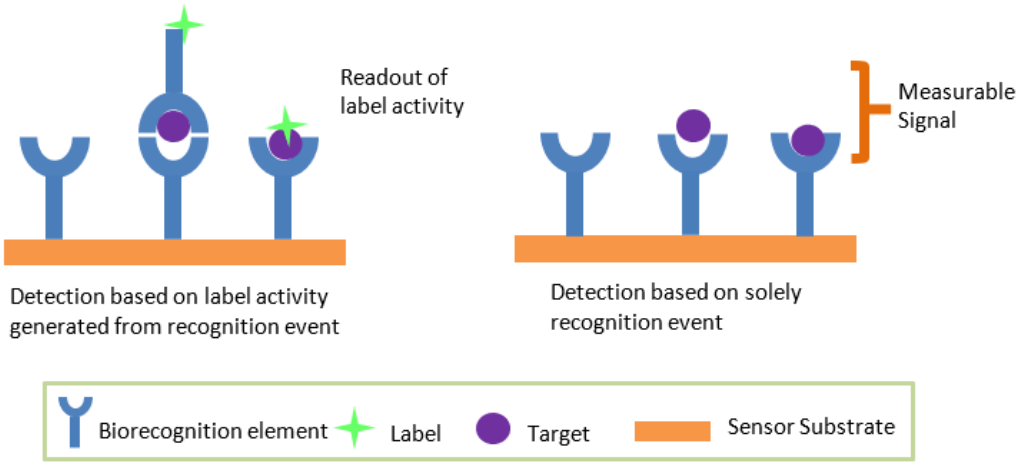

Figure 1-4 Schematic for (a)label free (b) label-based sensing mechanism (adapted from [14] with minor modification)

Optical label free sensing can be performed through a variety of transduction signal such as absorbance, transmission, polarization, reflectivity, refractive index (RI) and Raman scattering. Sensing technologies based on refractive index has been growing in recent years. Different optical structures such as interferometers [15-17], waveguide [18], surface plasmon resonance [19-23], ring resonators [24-26], metallic nanohole array-based resonance [27], photonic crystal [28, 29] and optical fibers [30, 31] have used RI sensing in their operation. In general, this kind of sensors measure the RI change in the bulk solution caused by binding of the target analyte with the receptor molecule. The required detection volume is quite small as the RI signal scales with the analyte bulk concentration or surface density rather than the total amount of the analyte.

Photonic crystal in particular is widely used in microfluidic devices due to their low detection volume requirement and ease of fabrication and integration into

microfluidic devices. A lot of studies done so far involving PCs in microcavities has reported to have achieved better Q factor and hence better sensitivity and detection limit [29]. 2D PC sensors have demonstrated good performance for liquid sensing. In this dissertation we have used a 2D free space couple PC sensors for gas sensing. The PC sensor is integrated with μGC enabling the system to separate and identify complex volatile organic compound (VOC) mixtures, a feature it lacks when used on its own. Polymer coating on the PC sensor experiences a refractive index change on interaction with VOC causing a shift in the Fano resonance peak of the PC. Integration of the sensor with a fully automated μGC system offers a promising portable, cheap and user-friendly VOC analyzing system.

1.4 Organization of dissertation

The dissertation includes six chapter which have been organized in the following manner:

Chapter 1 gives an introduction of the μGC system and photonic crystals along with motivation for this research. Here we discuss the features offered by the technologies and why it is important to integrate them to achieve vapor sensing.

In chapter 2, a glimpse of the current state-of-art in 2D PC based gas sensors is provided. Application of different kinds of 2D PC sensors are discussed along with their pros and cons. Additionally, the 2D PC optical characteristics and Fano resonance are described in more detail.

A literature review on the current trends in μGC is provided in chapter 3. It talks about the miniaturization of individual components and the system as a whole.

Chapter 4 focuses on characterization of the µGC system using a well-established electrical sensor called the photo ionization detector. Individual components of the µGC system are also characterized to obtain optimum performance. The µGC system is used to detect lung cancer biomarkers and workplace hazardous VOCs. It is also integrated with a mass spectrometer to analyze real breath samples.

Experimental results on integration of the µGC system with a PC sensor to analyze VOCs is covered in chapter 5. Key sensing metrics like Q factor, detection limit and sensitivity are discussed. Chromatogram showing separation and detection for 10 VOCs identified as workplace hazardous VOCs is provided. Also, separation performance of an on-chip vapor sensing platform formed by the integration of PCS sensor to an microfabricated silicon column is reported.

Chapter 6 concludes the dissertation and suggests future research prospects. It highlights the findings of this research project along with talking about the directions that this project could be developed in.

Chapter 2

Overview of Photonic Crystal Based Gas Sensors

2.1 Introduction

Photonic Crystal (PC) employs periodicity of refractive index contrast to manipulate the propagation of light. Strong light-mater interaction, lithographic tunability and small footprint makes it a promising technology to be used for any kind of sensing. Consequentially, PC of different dimensionality and dielectric material combination has found application in a gamut of applications in today's world. Some of the sensing applications are refractive index sensors [32, 33], gas sensors [34-37], liquid sensors [38, 39], temperature sensors [40], stress sensors [41], humidity sensors [42, 43], biochemical sensors [44-46]. Here we are going to describe the use of different kinds of 2D photonic crystal in gas sensing instances along with elaborate discussion on the band structure and Fano resonance seen in 2D PC sensors.

2.2 2D Photonic Crystal Based Gas Sensor

Photonic Crystal gas sensors can be implemented either through defect based or defect free photonic crystal. Defect based structure has some form of modification performed on the device that break the periodicity of the structure. These modifications affect the dispersion diagram and allow some of the mode to propagate in the bandgap. Mode volume, sensitivity, quality factor and limit of detection are key parameters of any gas sensing technology. Quality factor is proportional to the amount of energy stored in the optical cavity. In PC slab structure vertical confinement is compromised due to dissimilarity between the upper cladding (air) and the bottom cladding (buried oxide)

[47]. This is represented by Q_{ver}. Likewise, light is lost in the horizontal direction due to the finite number of layers encompassing the defect, Q_{lat}. Hence the overall quality factor, Q can be defined by

$$\frac{1}{Q} = \frac{1}{Q_{ver}} + \frac{1}{Q_{lat}} \tag{2.1}$$

Mode volume is related to the volume of the cavity through the following relationship [48]:

$$V_{mode} = \frac{\iiint d^3 \in (\vec{r})|E_{mode}(\vec{r})|^2}{max\{\in (\vec{r})|E_{mode}(\vec{r})|^2\}} \tag{2.2}$$

where $\in (\vec{r})$ is the refractive index variation in space and $E_{mode}(\vec{r})$ is the electric field profile of the mode.

Sensitivity, S can be defined as the ratio of change in resonance wavelength with respect to change in refractive index. Optical gas sensors often express sensitivity in terms of change in resonance wavelength per change in concentration or mass unit. Detection limit, DL or the lowest value of change in wavelength that can be tracked is a tradeoff between sensitivity and quality factor as described by

$$DL \propto \frac{1}{Q.S} \tag{2.3}$$

2.2.1 Photonic Crystal Cavity

PC cavity sensors are designed by creating either an acceptor or a donor type point defect or alternatively establishing optical confinement in a small area through structural modification. They generally have lower mode volume and is more effective in

sensing small amount of sample in comparison to its counterpart. A Cryptophane E infiltrated defected PC side coupled cavity structure using fiber ring-down technology for demodulation of PC resonance spectrum with high precision was demonstrated by Qian et al (Figure 2-1(a,b)) [49]. Simulation showed refractive index sensitivity of 450 nm/RIU, quality factor (Q-factor) of 10^4 and a methane detection limit of 2.37 ppm. The infiltrating molecule is only selective to methane and hence is not sensitive to any other gaseous analytes. Experimentation would have given a better estimate of its performance. Another silicon PC microcavity with air slot was fabricated and demonstrated showing a Q-factor of 32,900 and sensitivity of 421 nm/RIU as shown in Figure 2-1(c,d) [50]. Application in sensing nitrogen, hydrogen, and carbon dioxide experimentally revealed a detection limit of $1x10^{-5}$ RIU.

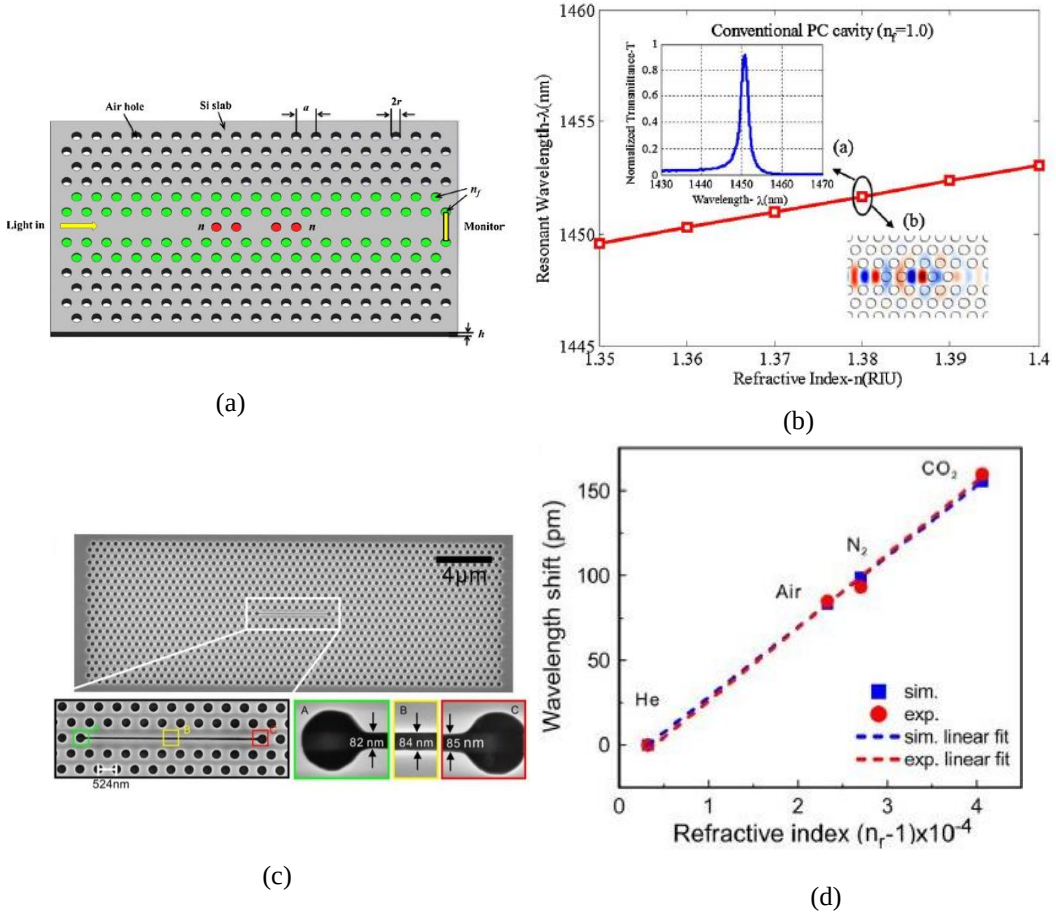

Figure 2-1 (a) Basic structure of a slow light engineered PC cavity, in which the central four holes are infiltrated with cryptophane E, and the first two rows of air holes are infiltrated with suitable fluid for slow light optimization (b)Variation of resonant wavelength along with the refractive index n that infiltrated in defected holes of conventional PC cavity (n_f= 1.0), while the inset (a) and (b) show the transmission spectrum and corresponding steady-state electric field distribution when n = 1.38. [49] (c) SEM image of an L9 slot cavity, a magnified view of the slot cavity is in the left lower panel; zoomed views of region A, B, C are shown in the right lower panel (d) Experimental results of the L9 slot microcavity as a gas sensor. The relationship between the resonant wavelength shift and gas RI. The resonance wavelength for He is used as a reference. The experimental sensitivity is 421 nm/RIU, which is determined by a linear fit (red dashed line). The standard deviations of resonant wavelengths for He, Air, N_2, and CO_2 are 0.0014, 0.0012, 0.0014, and 0.0011 nm, respectively [50]

2.2.2 Photonic Crystal Waveguide

In case of a line defect in the periodic structure of a PC it is referred as PC waveguide. Here the light is confined laterally by the PC while vertically by the total internal reflection. Hence only a certain frequency range of light can be transmitted through the waveguide [51]. A slotted PC waveguide exhibited gas sensing capacity by selectively impregnating two rows of holes with different refractive index liquid [36]. This structure created on silicon-on-insulator (SOI) demonstrated a detection limit of 1.56 ppm (CO_2) and was found to be sensitive to carbon monoxide, carbon dioxide and hydrogen sulfide by adjusting the refractive index of the liquid to match the absorption peak of the analyte under investigation (Figure 2-2(a,b)). Researchers have attempted to increase the interaction between light and gaseous analyte by modifying the slow light property of PC structure with ring shaped hole (Figure 2-2(c,d)). A ring-shaped hole based PC waveguide structure with holes etched in the waveguide region was reported with gas sensing simulated results [52]. Along with investigating the effect of ring etch depth a 513 nm/RIU sensitivity was published for 50 nm over etching in buried oxide layer. Several gases like nitrogen, hydrogen, ammonia, and oxygen were applied to the structure. Unfortunately etching of the silicon dioxide layer over a specific thickness reduced the sensitivity.

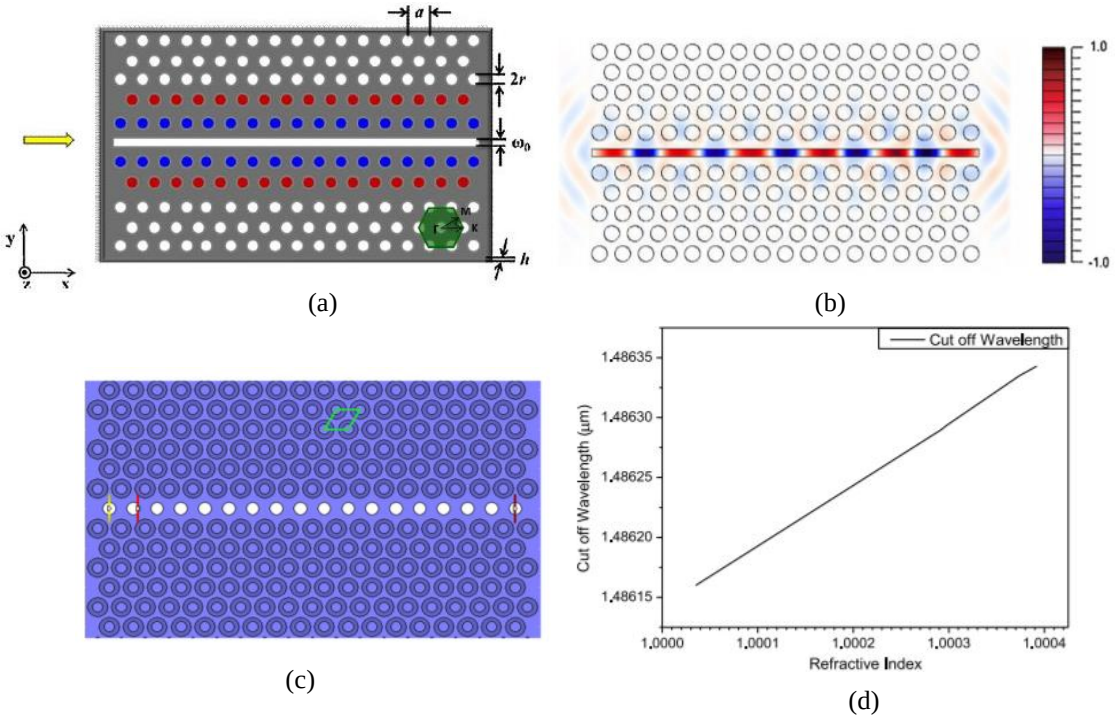

Figure 2-2 (a) Basic structure of SPCW, where a is the lattice constant, r is the radius of air hole, w_0 is the slot width and h is the thickness of the slab. The blue colored holes are infiltrated with liquid with refractive index of n_1 and the red colored one with liquid of refractive index n_2 (b) Electric field distribution of the basic SPCW [36] (c) Schematic of ring shape hole-based PC waveguide with a row of holes within the waveguide (d) Shift in cut-off wavelength of the PC waveguide with the change in refractive index [52]

2.2.3 Photonic Crystal Slab (PCS)

In comparison to the 2D defect-based PC, defect free PC like a PC slab has advantage of flexible alignment requirements, straightforward fabrication process with more tolerance to deformation in the lattice structure and adaptable to multiplexed operation. There has been a lot of work on application of defect free PC for biosensing but relatively limited number of works on vapor sensing. We have explored a defect free Si PCS on SOI for vapor sensing in our previous work (Figure 2-3 (a,b)) [37]. 57 ppm detection limit was established for hexane. However, response time for the sensor was on the order of 100 s as a consequence of large gas cell and dead volume. The long response

time is inadequate to be used as real time detector in a μGC system. Despite of a good number of PC based work demonstrating good Q or S in gas sensing applications, all kinds of PC suffer from certain drawbacks. Its primary limitation is absence of detection specificity. Some of these research work has addressed this issue by modifying either the instrumentation or elements of the structure itself [36, 49, 53, 54]. However, the process is labor intensive and prone to error. In some cases, the results are difficult to interpret. This deficiency can be compensated by integration with gas chromatography system. Coupling PC with optical fiber often presents with issue due to modal mismatch [55]. We could resolve this problem by using free space coupling to supply/collect light to/from the PC structure. Another pressing challenge is integration of PC with microfluidics efficiently. Transfer printing of photonic crystal from SOI substrate to other types of substrates like glass and anodic bonding between different substrates is a potential solution.

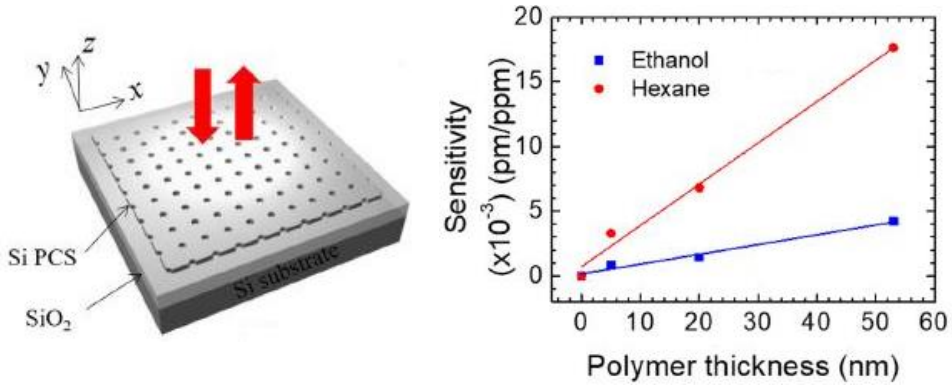

(a) (b)

Figure 2-3 (a) Schematic view of a PCS vapor sensor with free-space coupled laser beam (b) Sensitivity of the PC slab sensor to hexane and ethanol vapor with different polymer thickness [37]

2.3 Photonic Band Structure

Constructive and destructive interference caused by reflection and refraction of photons at the boundary of the contrasting RI material results in generation of photonic band in the periodic structure [56]. It can be defined as a range of frequencies that can propagate though the lattice. Similarly, photonic band gap (PBG) denotes the range of optical wavelengths that cannot pass through the photonic crystal. This propagation is determined by the polarization and direction of propagation of the incident wave. Photons possessing frequency within the band gap range are reflected by the material and can only enter the PC evanescently. Figure 2-4 shows the band structure for different types of 2D PC [57].

Maxwells equation are used to describe the photonic band structure of PC. They are:

$$\nabla \cdot \mathbf{B} = 0 \qquad \nabla \times \mathbf{E} = -\frac{\partial \mathbf{B}}{\partial t} \qquad (2.4a)$$

$$\nabla \cdot \mathbf{D} = \rho \qquad \nabla \times \mathbf{H} = -\frac{\partial \mathbf{D}}{\partial t} + \mathbf{J} \qquad (2.4b)$$

here ρ and **J** are the free charge and current densities and **E, D, B, H** represent electric, displacement, magnetic induction, and magnetic field respectively. All these variables are time and position dependent.

For non-magnetic, non-dispersive, linear, and isotropic dielectric material **E** and **D** along with **H and B** are related through constitutive relation**s:**

$$\mathbf{D} = \varepsilon\varepsilon_0\mathbf{E} \qquad (2.5a)$$

$$\mathbf{B} = \mu_0\mathbf{H} \qquad (2.5b)$$

where ε is the dielectric function (of time and position) and ε_0 and μ_0 are the permittivity and permeability constants of free space. Combining equation (2.4) and (2.5) with the assumption of harmonic time-dependence for the fields at any given frequency, the wave equation for PCs can be derived:

$$\nabla \times \left(\frac{1}{\varepsilon(\mathbf{r})} \nabla \times \mathbf{H}(\mathbf{r}) \right) = \left(\frac{\omega}{c} \right)^2 \mathbf{H}(\mathbf{r}) \tag{2.6a}$$

$$\mathbf{E}(\mathbf{r}) = \frac{i}{\omega \varepsilon_0 \varepsilon(r)} \nabla \times \mathbf{H}(\mathbf{r}) \tag{2.6b}$$

where ω is the angular frequency of propagating light. The distribution of magnetic field within a PC is fully determined by the solutions of equation (2.6a), and electric field can be calculated with equation (2.6b).

Solution of equation (2.6a) determines the photonic band structure of PC. It is an eigenvalue equation, and depending on ε(r), both discrete solutions and bands of solutions may exist. When equation (2.6a) is satisfied over a continuous range of frequencies, a photonic band appears. PBG is an uninterrupted range of frequencies for which equation (2.6a) cannot be solved (for the given ε(**r**)). A discrete solution to equation (2.6a), corresponding to a specific isolated frequency, denotes a confined optical cavity state within a PBG at that frequency. However, equation (2.6) cannot be solved analytically for practical PCs, thus researchers depend on numerical (computational) modeling to make predictions about the PC behavior.

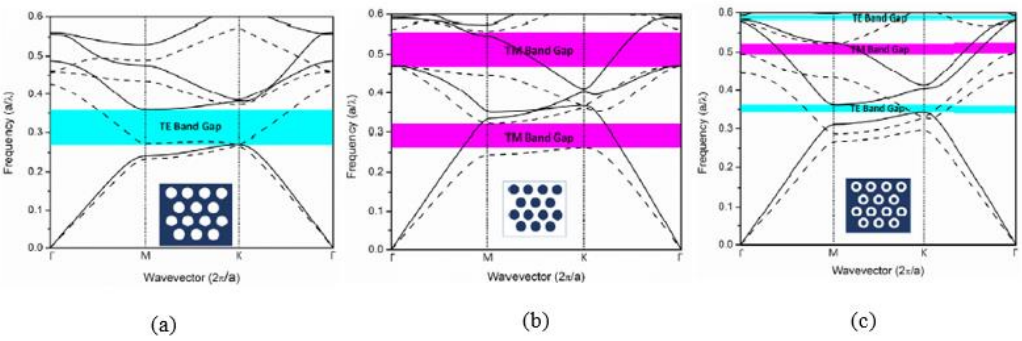

Figure 2-4 Band structure of (a)hole-type PC, (b) rod-type PC and (C) ring-type PC structure. The structure was designed on a dielectric slab of RI 2.805 having the following design parameters: lattice period, a = 473 nm, hole or rod radius, r = 0.35a, ring outer r radius, r_{out} = 0.45a and ring inner radius, r_{in} = 0.24a. Insets show the lattice of the structure considered. The cyan-colored band indicates the bandgap for TE polarization and the magenta-colored band indicates the TM bandgap [57]

2.4 Fano resonance in 2D PCS

Originating from atomic physics, Fano resonance is the product of constructive and destructive interference of discrete resonance states with broadband continuum states [58]. This phenomenon, being common in many aspects of physical sciences, has been found in many nanophotonic structures, such as quantum dot, PC, plasmonic, and metamaterials [59, 60]. In contrary to conventional symmetric-shaped Lorentzian resonance, Fano resonance possess asymmetric line profile [58, 59]. It originates from a close coexistence of resonant transmission and resonant reflection and can be reduced to the interaction of a discrete (localized) state with a continuum of propagation modes. The sharp dip-to-peak transition of Fano resonance makes it applicable in a wide range of photonic devices such as optical filters, switches, sensors, detectors, etc.

When light shines on a PCS from out of the plane direction (*e.g.*, surface normal direction), there are two pathways for energy transportation. The first pathway is a direct transmission process, where a portion of the incident energy goes straight through the slab and generates the initial pulse. The second pathway is an indirect transmission process, where the remaining portion of the incident energy excites the guided resonance and subsequently leaks out to free space. Having considered the interference between these two pathways, the transmitted amplitude t and the reflected amplitude r can be expressed as [61]:

$$t = t_d + f\frac{\gamma}{i(\omega - \omega_0) + \gamma} \tag{2.7a}$$

$$r = r_d \pm f\frac{\gamma}{i(\omega - \omega_0) + \gamma} \tag{2.7b}$$

where t_d and r_d are the direct transmission and reflection coefficients, ω_0 and γ are the center frequency and width of the resonance, and the factor f is the complex amplitude of the resonant mode. The plus and minus sign in equation (2.7b) correspond to even and odd resonant modes with respect to the mirror plane parallel to the slab. For $0 < |t_d| < 1$, equation (2.7a) gives a Fano line shape sharp dip-to-peak transition.

Fano resonance in 2D PCS arises from the coupling of in-plane guided resonance modes above the light line to the out-of-the-plane radiation modes due to phase-matching provided by the periodic lattice structure. Using Fano resonance in sensing applications is an alluring concept since it provides an efficient and easy way to channel light from in-plane to free space. Additionally, the asymmetric Fano line shape in the reflection and transmission spectrum of 2D PCS is advantageous for extracting small spectral shift induced from small RI change around the slab, and thus better DL can be achieved.

Chapter 3

Overview of Micro gas Chromatography

3.1 Introduction

The increasing need for analyzing and identifying chemicals in environmental, defense, health and beauty applications have led to the popularity of micro gas chromatography (μGC) systems. According to recent trends, unlike what its name suggests, these group of instrument includes all portable gas chromatography system irrespective of its fabrication technique or weight. The key features of such a system are compact, automatic, reduced power consumption, minimal production and maintenance costs and suitable for field analysis. Thus, it provides the advantages of rapid analysis and turnaround time as well as simpler sample preparation and introduction mechanism reducing the probability of modifying the original sample. Over the last decade researchers have invested their efforts in making these systems more efficient and suitable for mass use.

Over time miniaturization and integration in GC has been noticed both on component and chip level. Hybrid integration involves fabrication of individual component and then establishing fluidic connection between them using microfabricated or off the shelf connectors. Although this process offers flexibility of modifying or repairing one component without touching the rest of the system it is a time and labor-intensive process. Since each component is fabricated separately the fabrication costs will also be higher making it unsuitable for mass production. Such a system is also prone to cold spots along the fluidic connections which could distort the peak shapes and degrade the overall performance of the system. In case of monolithic integration all the

components are fabricated on the same chip presenting a solution to the drawbacks of hybrid integration. However, this process comes with its own set of challenges. Since all the components are fabricated at the same time if one of the components is defective the whole chip becomes unusable. Also, higher fabrication cost and design constrain would be involved for thermal and electrical insulation between components. In this overview we have shone light on the variety of research work published in the last two decades on each component of a μGC system. Gas chromatography system consists of three major segments-sampling and focusing, separation of analytes, and finally detection of the separated analytes. Here we have discussed the research efforts in miniaturization of each of these components individually and then as an integrated system.

3.2 Injector

The sample introduction process focuses on delivering the sample to the column inlet with minimum amount of dilution and in certain cases with higher concentration compared to the original sample. Once the sample is injected into a benchtop GC all or part of it is usually driven to the column by pumps, valves and pressure regulators depending on the mode of injection (split or split less). Large dead volumes and sample volumes makes sample plug broader as it passes through these parts. Any amount of sample leakage will only worsen the situation. μGC attempts to resolve this problem by redesigning the sampling mechanism both fluidically and thermally.

In 2012 Nachef and her colleagues introduced a micro injector with 250 nL sample volume that integrated six low leak PEEK microvalves for natural gas analysis. Each valve is fabricated from stacks of silicon, silicon-on-insulator wafers and a PEEK film. The valves are triggered pneumatically by applying pressure on the PEEK film

through actuation holes. Transition time of less than 35 ms between the sampling mode and the injection mode and low leakage levels ensured reliable and repeatable sample injection. The response time could be further reduced by optimizing the valve triggering system response. PEEK having excellent thermal and chemical stability has proven to be a good material suitable for harsh environments and high temperature.[62]

The test sample for GC is not always available in gas phase and might be required to be extracted from an aqueous phase. A simple solution to these was proposed in 2000 by using membrane extraction with sorbent interface (MESI) in a commercial μGC system. It consisted of a selective flat sheet silicone polycarbonate membrane, nafion water trap and a sorbent interface that trapped and concentrated volatile organic compounds (VOCs) present in an aqueous sample. Compared to direct injection, MESI showed to two times larger sensitivity with just a sampling time of 1 min. But this structure is incompatible to a microfluidic system [63]

A reconfigurable micromachined injector having two symmetrical dosing loops offered sampling volume of 12-14 μL. The glass-silicon-glass chip is operated by a pneumatically operated microvalve. Teflon coated thin polyimide foil acts as the microvalve actuator for the injector. Simple fabrication process allows for the fast microinjector (17 ms) to be redesigned with ease and speed [64]. Another recent innovation in sample transport is the use of Knudsen pump (KP) that operates on the principle of thermal transpiration. Absence of moving parts make this technology suitable for continuous operation reliably without any supervision. Temperature difference between a heated top and passively cooled bottom plate drives the flow in the Knudsen pump placed in between. KP arrays made of a mesoporous polymer having a high nano-

channel density (10^{11}/ cm^2) has been reported to provide flowrate up to 1 mL/min and 0.26 mL/min with helium and dry air respectively as carrier gas. Pressure programming of the KP array not only improved the chromatographic resolution but also reduced the analysis time. Further miniaturization initiatives for KP to achieve higher pumping pressure and flow rate are still pending [65]. Aqueous samples were made compatible for GC analysis using a purge and trap technique in 2014. Akbar et al developed a micro purge extractor chip combined with a micro thermal injector to collect and analyze VOC from water sample with a detection limit of 500 ppb. Aqueous sample is flown through the micro purge extractor chip while a steady supply of purified nitrogen purges the water organic compounds (WOCs) and deliver them to the micro thermal injector chip connected in tandem. The thermal injector has micro posts coated with a layer of Tenax TA that traps the incoming WOCs (Figure 3-1(a)). On completion of extraction time the thermal injector was heated to release the trapped WOCs as helium sweeps them out to the GC column for separation. The highest percentage of recovery using this system is 38% for ethylbenzene. Reduced pressure drops and power consumption comes at the expense of lower purging flow rates (0.4 mL/min) which is a major limitation for improvement in the recovery rate. Modification in the chip design and experimental conditions are underway to remove this limitation and make this chip more efficient for field analysis [66].

A two-stage bidirectional Knudsen pump was demonstrated by Qin and his colleagues in a completely electronic μGC system with average power consumption of 3.2 W (Figure 3-1(b)). The pump is composed of mesoporous mixed-cellulose-ester membranes stacked between microfabricated glass dies. Average temperature and

temperature difference along the membranes determine the flow rate of the pump which can go up to 0.5 sccm. Since temperature gradient is very important for the proper functioning of this pump optimization in the experimental conditions might be required to adapt it to field use [67]. Lu et al developed a chemically inert microvalve module that can perform up stream flow routing between one sampling path and multiple separation paths. The module brings together 3 microvalves made of fluidic die stack, polyimide valve membranes, thin film heater and solenoid actuators all placed in a customized 3D printed housing (Figure 3-1(c)). They demonstrated a lifetime of greater than 500 cycles over 330 hours without any performance degradation and a response time of 120 ms. A temperature of 75 °C can be maintained on the valve just by using 1W heating power. Comparison of performance with a commercially available valve show that it does not causes any peak distortion by retaining and in some cases help to reduce the peak width due to its ability to perform heated injections into a GC system. An undemanding fabrication process for the microvalve module makes it a promising sampling system for μGC system [68]. A microfabricated silicon chip was developed recently to allow solid phase extraction of VOCs from aqueous samples. The chip contains squared micro pillars coated with a thin layer of porous SiOCH that extracted the VOC present in an aqueous sample as it passes through it. Prior to a drying period after extraction time resistive heaters sputtered at the back of the chip heats up the extraction phase to release the VOCs onto the carrier stream. The automated chip was used to extract polycyclic aromatic hydrocarbons from water samples with the entire protocol of extraction, drying and desorption being completed under 25 min. On average the device exhibited a 44% extraction rate from the water sample and did not leave any residue. However the

stability of the coating over multiple extraction, during and cooling cycle needs to be investigated for long term validity of the data [69]. In 2020 Zampoli introduced a GC platform, components of which were integrated using only MEMS technology. The injector used for sampling was implemented through five microvalves which were pressure actuated by a single external pilot valve (Figure 3-1(d)). They were microfabricated using stacks of silicon wafers bonded together using SU-8 as adhesive which also serves as the valves membrane that determines the status of the valve. The injector is heated using flexible polyimide/copper heaters and show no damage after multiple hours of operation at 200 °C. Use of SU-8 as the membrane material allows simpler fabrication process for the valves along with reduced dead volumes, higher packing density and a robust structure [70].

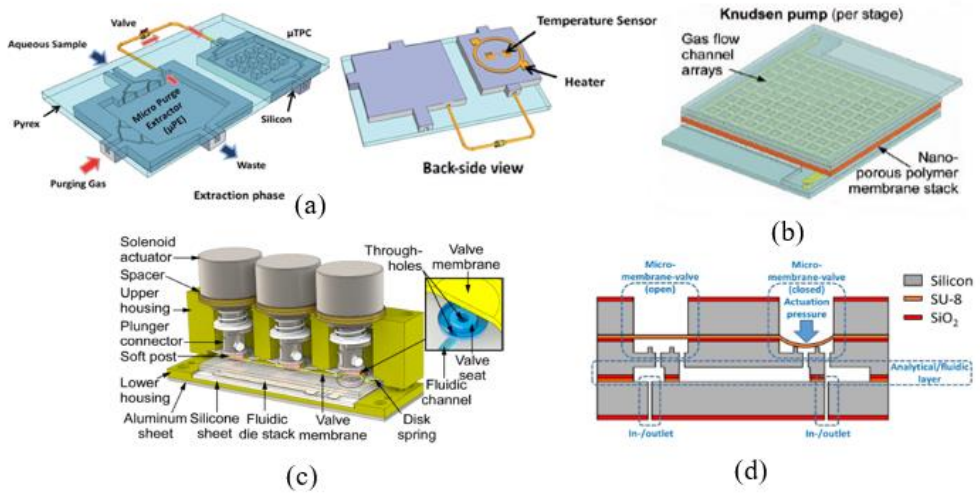

Figure 3-1 (a) Conceptual diagram showing the topology for the extraction and analysis of water organic compounds. A back-side heater is utilized for thermal desorption of analytes from the mTPC for chromatographic analysis [66] (b) iGC3.c2 system architecture and component design [67] (c) The architecture of the microvalve module. The microvalve on the right is in the open state, whereas the other two of the microvalves are in the closed state [68] (d) Simplified schematic representation of the cross-section of the 3-wafer MEMS stack implementing the injector used in this work [70]

3.3 Preconcentrator

Preconcentration is often a part of μGC systems focused on identifying and analyzing dilute samples. It offers two important benefits. Accumulation of analyte within the preconcentrator structure permits enrichment of the sample while difference in affinity for analytes provides for the discrimination capability. The process is characterized by two distinct phases. First, the bed of adsorbent is exposed to target analyte where the adsorption reaction takes place. Then the adsorbent material is heated up to release the chemicals downstream. This is the desorption reaction. Preconcentrator can be based on either fractional or complete trapping of VOCs. Devices that rely on equilibrium between the VOC concentration in the carrier stream and that on the adsorbent surface usually captures only a fraction of the sample. Complementing these are other preconcentrators which capture the sampled VOCs completely. While these are bulky and consume higher power, their preconcentration factors are generally higher in value compared to the preconcentrators that trap partially [71, 72]. On the other hand, significant improvement in sensitivity is demonstrated by partially trapping of VOCs although their preconcentration factors is miscalculated due to loss of information on how much of the total sampled VOC was actually adsorbed [73].

The commercial thermal desorption tubes available in market are generally ¼" stainless steel or glass tubes which need to be connected to GC systems with standard metal connector. Amount of adsorbent required to functionalize them is in order of grams and the power required to heat them up is significant. Possibility of dead volumes and sample leakage is highly likely in such a structure [74, 75]. Adsorbent material

characteristics, sampling condition, preconcentrator geometry, heating arrangement are factors that affect the preconcentrator performance significantly. Their performance is often characterized by determination of preconcentration factor, breakthrough volume, peak width, pressure drop, power consumption.

Preconcentrator with multiple adsorbents have become widely popular. A three-stage silicon micro preconcentrator was fabricated by Tian and his colleagues that could effectively concentrate analytes with volatility up to 4 orders of magnitude. Material characteristics of the adsorbent like surface area, pore morphology and pore size distribution allow them to have more affinity for a group of chemicals with certain volatility. Carbopack B, Carbopack X and Carboxen 1000 was used in this case to trap and release 30 common VOCs with 100 % desorption efficiency. In case of multistage preconcentrator the order in which the adsorbents are placed in the preconcentrator is also crucial. Trapping of high volatility chemicals is favored by large surface area of adsorbents. So larger surface area adsorbents are placed downstream in the sampling flow path to avoid trapping low volatility compounds. In comparison to its single stage counterpart the dead volume (from 8.16 to 2.62 µL/stage), thermal mass (from 28.6 to 10.1 mg/stage), heating rate (from 18 to 100° C/s) and pressure drop (from 13.80 to 2.11 KPa/stage) in the three stage preconcentrator shows remarkable improvement. All the analytes were separated completely with peak width less than 2.05 s with the preconcentrator consuming 1.5 W power. However, a 3-mask process for just the cover plate along with the fabrication protocol for inlet/outlet adapter ring and the adsorbent chamber makes it a complex and time-consuming fabrication process [76]. A variety of adsorbent materials other than graphitized carbon has been explored in µGC. These

include carbonaceous adsorbents (carbon nanotube and nanoporous carbon), zeolite, polymer and organosilicas [77]. The distinct crystalline pore structure of zeolite allows them to have good selectivity and strong adsorption affinity making them excellent option as adsorbent for trace concentration samples. They also offer long term durability, high thermal stability, so that even analytes with less volatility could be analyzed without reduction in performance. To trap an explosive related compound, orthonitrotoluene a micro preconcentrator based on dealuminated Y-type zeolite (DAY) was developed. A 20 µL rectangular silicon cavity (5 mm x 10 mm) furnished with micro-pillars housed the adsorbents with heater resistor fabricated on the back of the cavity (Figure 3-2(a)). The detection limit was reduced from 1 ppm to 0.37 ppm with zeolite as adsorbent. Also, adsorption/desorption performance of the zeolite is not affected by other interferents like humidity and toluene. Preconcentration factor of ~7 was reported in this project [78]. Carbon nanotube sponge (CNT) has been utilized as adsorbent in preconcentrator (Figure 3-2(b)). This form of CNT exhibits the innate properties of multiwalled CNT such as hydrophobicity, high porosity, mechanical strength, thermal conductivity along with a 3D maze-like network that favors trapping of VOCs. On occasion of using, it in a standard thermal desorption tube in GC moderate preconcentration factor (200-300) was shown with 96% desorption efficiency [79]. The adsorbent showed uniform heating and had the option of being heated by applying a potential through it directly instead of using a heater. Narrow desorption bandwidth (0.74 s) and fast heating rates make it a promising candidate for micro preconcentrator [80]. CNT foam was used in a microfabricated preconcentrator by Lee et al to detect ethane at low concentration (Figure 3-2(c)). Comparison with carbon molecular sieve adsorbent showed five times reduction in

pressure drop and three times higher preconcentration efficiency. Later the same group introduced metal organic framework embedded metal foam (MOFM) as adsorbents [81]. This class of material has high specific surface area, low desorption temperature and thermal stability in addition to high thermal conductivity and low pressure drop generally offered by metal foams. The micro-preconcentrator could be desorbed completely at a low temperature of 150 °C and showed 4 times better preconcentration factor in addition to 3 times lower pressure drop compared to a commercial carbon-based adsorbent (Figure 3-2(d)).

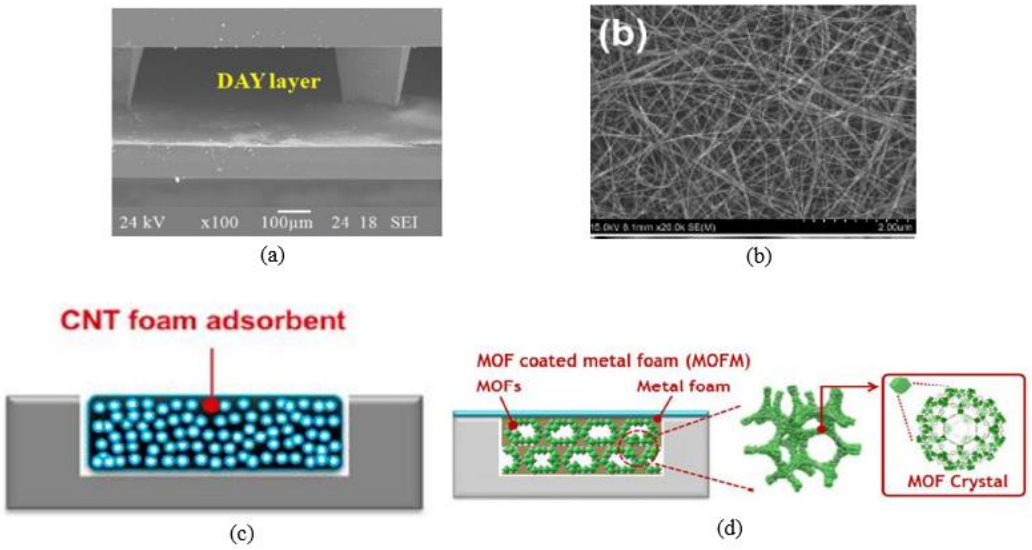

Figure 3-2 (a) SEM image of DAY layers deposited on the micro-preconcentrator cavity [78] (b) photograph and SEM image of CNT sponge [79] (c) Schematic diagram of cross-sectional view of adsorbing chamber filled with CNT foam [80] (d) Cross-section of adsorption chamber packed with MOFM adsorbent [81]

Another silicon-glass micro preconcentrator embodying high aspect ratio micro posts covered in Tenax-TA polymer adsorbent has been discussed for air pollutant

detection. The Tenax-TA layer had higher affinity for VOCs with high boiling point and could retain 30-400 ng of analytes depending on its affinity toward the analyte. Breakthrough volume analysis shows that benzene has the least breakthrough volume (1 mL) followed by toluene (13 mL) while the rest of the chemicals had breakthrough volume more than the typical sampling volume. An interesting flow manipulation approach was used to reduce the peak width from 4 s to 0.8 s. In this technique the preconcentrator is initially heated without carrier gas flow and then carrier gas is flown through it once the chip temperature reaches 200°C making the desorbed peak sharper than the regular desorption technique. The peak width could be further reduced to 0.35 s with higher carrier gas flow rate. Desorption efficiency of 99% was achieved in this technique and any remaining analyte was removed through a purging cycle in between analyte runs. Comparison with a conventional sorbent tube loaded with Tenax TA shows that the sample volume and sampling time required to collect enough analyte is at least 3 orders of magnitude higher compared to the micro preconcentrator. Further modification to the chip is required to trap the low boiling components of hazardous pollutants like gasoline [82]. An extensive characterization of dual cavity and single cavity microfabricated preconcentrator was published in 2015. The dual cavity preconcentrator accommodates Carbopack B and Carbopack X adsorbent while the single cavity preconcentrator held one of the two at a time. Tapered wall near the inlet/outlet favors even flow distribution and decreases turbulence. The chips are supplied with resistive temperature devices (RTD) for resistive heating and temperature monitoring. Effect of changing split ratio after preconcentrator between the analytical path and the waste channel, flow rate, analyte concentration and volume on resolution, sensitivity,

breakthrough volume and peak width of the preconcentrator was explored. They also introduced a modified preconcentration factor calculation method using the ratio of the collected sample volume to the volume having the same mass of analytes at the point of detection. This approach provides a more practical mode of calculation since all analysis will include a separation stage before detection. The dual cavity micro preconcentrator demonstrated a preconcentration factor of 200-1600 for ~20 analytes within a vapor pressure ranging 3 orders of magnitude with a sampling time of less than 5 min [83]. An 'U' shaped glass micro preconcentrator connected to the rest of the system through a cantilever structure showed an effective way of alleviating thermal stress and heat loss (Figure 3-3(a)). Two kinds of Carbopack adsorbents are packed in the lower half of the channel held in place by micro fabricated pillars and glass beads with the channel itself cantilevered above a glass spacer. This ensures thermal isolation of the device from the substrate. Temperature profile of the preconcentrator is shown in Figure 3-3(b). Sampling of sub-ppm level indoor pollutants was completed in 30 min at a sampling rate of 0.2 mL/min using ambient air as carrier gas [67].

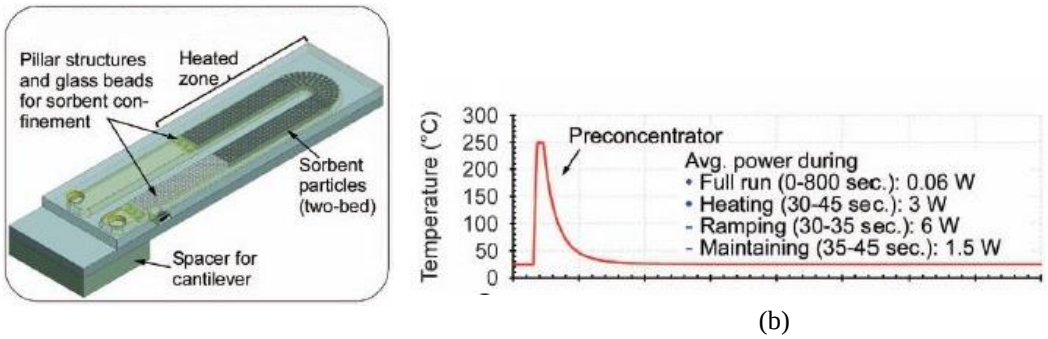

(a) (b)

Figure 3-3 (a)Preconcentrator design in iGC3.c2 system (b) The preconcentrator temperature during a typical thermal pulse to perform vapor injection [67]

Researchers are now progressing towards fabrication procedures that are easy and less time consuming. An inkjet printed foil gas preconcentrator on a polyimide substrate is one step towards that goal [84]. Moving away from rigid substrates this research work has introduced a fabrication technique for preconcentrators using a flexible foil that is both cost effective and reproducible. A gold micro-hotplate is first printed on a foil which is then rolled, sealed, and filled with adsorbents (Figure 3-4(a)). As the micro hotplate is lining the interior wall of the preconcentrator heat dissipation is minimum. However, the diameter of the preconcentrator (1 mm) is quite large to be suitable for a µGC configuration. Also, the preconcentration factor demonstrated (68 for Carbopack-Benzene combination) quite low compared to other preconcentrators that we have reviewed so far. Simulated temperature profile for the heater is exhibited in Figure 3-4(b). Another silicon alternative substrate for preconcentrator was demonstrated in 2018. A metal gas preconcentrator was fabricated using laser etching technology and vacuum diffusion welding with an internal volume of 14.4 µL on a copper substrate (Figure 3-

4(c)) [85]. Copper having higher thermal conductivity and specific heat capacity compared to silicon is a promising substrate for this function. Moderate preconcentration factor (352 for 10 ppb isoprene) and relatively high power (~10 W for heating phase and ~3 W for isothermal phase) was reported for the microfabricated component. The heating efficiency could be further improved using a heater patterned on the chip rather than using an external ceramic heater. Thermal imaging in Figure 3-4(d) depicts the temperature profile of the heater. In addition to copper, glass has been used to fabricate preconcentrator. McCartney et al produced a fabrication friendly device on borosilicate glass wafers using wet etching with an integrated heater on the back side(Figure 3-4(e)) [86]. The chip exhibited good peak width (1.92-1.98 s) but for a very high desorption flow rate (25 sccm) which might be overbearing for a μGC system. Although comparison between with and without preconcentrator detector response revealed a low preconcentration factor (~5-13) the chip gave a good detection limit of 22 ppb for test analytes. The heat transfer model for the device is shown in Figure 3-4(f).

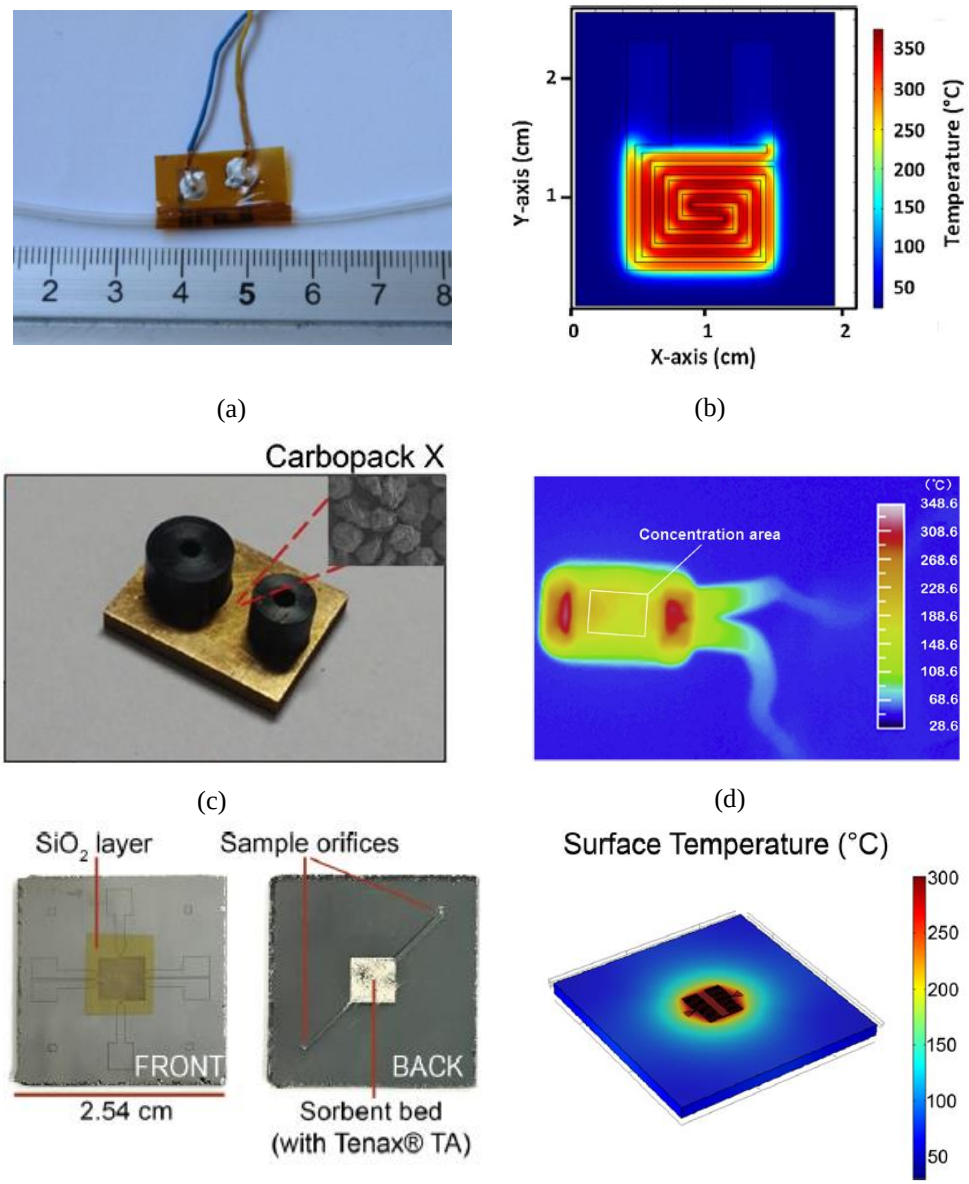

Figure 3-4 (a) Image of the rolled up foil preconcentrator with fluidic connection (b) Thermographic simulation obtained on COMSOL 4.2 of the micro-hotplate operating at a power of 1700 mW [84] (c) Actual image of the metal gas preconcentrator with inset showing the SEM image of the adsorbents (d) Thermal image of the metal gas preconcentrator using a commercial infrared camera [85] (e) Actual image of both faces of the glass preconcentrator (f) Model of the heat transfer. The power required to achieve a temperature of 260 C at the sorbent cavity was calculated to be 2.5 W [86]

3.4 Separation Column

Polyimide-clad fused silica capillary columns coated with a stationary phase is responsible for separation of analytes in a typical GC system. Differential interaction of the analytes with the stationary phase results in segregation of individual components from a mixture. As the analytes flow through the column, they partition at different rates between the mobile phase, meaning the carrier gas and the stationary phase which is the layer of polymer coating on the inside wall of the column. This rate is mainly dependent on the affinity of the chemical in the two phases. Consequentially, the time spent by an analyte in each phase is affected and hence the total time required to pass through the column is influenced. Thus, the compounds separated in time and space can be detected by a detector at the column outlet and identified based on their elution time and signal response. Microcolumns also work on the same principle with the added advantage of low power heating, small footprint, faster analysis, and enhanced separation performance.

Different column architecture has been investigated by Radadia et al (Figure 3-5). They concluded that serpentine column has higher separation plate number compared to circular-spiral and square-spiral for retained solutes under isothermal condition due to favorable hydrodynamic flow and uniform stationary phase coating. This work laid the foundation for evaluation of different microcolumns shapes and identified the favorable characteristics for a microfabricated column [87]. Variety of shapes and ratio of packing is used in columns to achieve higher sample capacity and ensure a stable and uniform flow dynamics. A semi-packed microcolumn with atomic layer deposited (ALD) alumina as a stationary phase showed good peak resolution under flow and temperature programming. The micro column yielded 4200 plates/meter under isothermal conditions

was able to separate 8 analytes in less than 1 minute. ALD is an innovative stationary phase deposition method that enables uniform deposition in high aspect ratio columns and also narrow width columns [88]. Simpler and inexpensive fabrication techniques like 3D printing is also being used for design and manufacture of microcolumns. Metals have unique properties like high mechanical strength and thermal conductivity and 3D printing offers freedom of design, complex geometry with high precision, rapid prototyping, and cost-effective customization-combination of these allows for manufacture of robust GC microcolumns with low column bleed that can be used at high temperature. A 1 m square spiral metal column demonstrated efficient separation performance of gas mixtures containing alkanes, aromatics, alcohols, and ketones within 3 min [89]. High viscosity, thermal stability, and low vapor pressure has made ionic liquids attractive stationary phases in gas chromatography. Regmi et al investigated the separation performance of a 1 m long semi packed column with an intermediate layer of aluminum oxide and ionic liquid as stationary phase. The silicon micro column showed a theoretical plate count of 8000/m at optimum flow rate. Separation performance of these columns was evaluated by separating complex mixtures of hazardous organic compounds, a sample of kerosene, diesel, and B20 biodiesel [90].

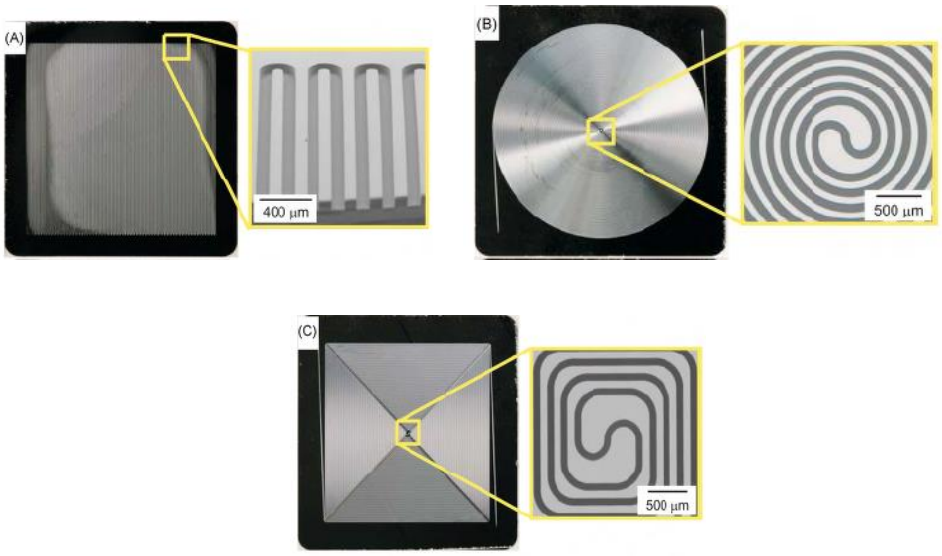

Figure 3-5 Microscope image of microfabricated silicon columns with (a) square spiral (b) circular spiral (c) Serpentine [87]

3.5 Detector

Several micro detectors have been researched for identifying the separated analytes at the end of the separation column. Conventional detectors suffer from the disadvantage of large sampling volume and dead volume leading to broadening of the peaks and slow response. When miniaturized, sensors offer a variety of favorable characteristics like small footprint, reduced dead volumes, low power consumption and minimal production and maintenance costs. Different technologies-electrical, optical, and mechanical has been explored to get these features.

Micro-photoionization detectors (µPID) work by ionizing analytes via UV light exposure and then collecting the ions to generate an electrical signal in response. Sun et al reported a µPID with ionization volume of 10 µL and detection limit of 1 ppb used in conjunction with a µGC column and micro preconcentrator. It is a nondestructive sensor

but can only detect chemicals that have ionization potential higher than what can be provided by the light source [91]. Bubble based gas sensor has been an interesting addition to gas sensing technology. Here a gas sample is first separated by a separation column and then the gaseous analytes are introduced into a liquid to form bubbles while the size of the bubbles is monitored using an optical camera. Size of the bubbles depend on gas types and mixture ratios with the carrier gas. Thus, by observing the variation of gas bubble sizes in reference to the background carrier gas bubble, a gas chromatogram can be obtained. The output stability of this technique was showed only 5.60% variation in 67 tests over a month. This is an easy to fabricate way to avoid the drawbacks of only physics or chemistry-based detector. However the post detection analysis is quite complex [92]. Infrared tunable diode-laser absorption spectroscopy is also promising optical technique for VOC detection. A 10 cm long nanoscale silicon waveguide structure exposed to the environment allows interaction of the analyte with the evanescent field of the near IR light introduced in it. The light collected at the end of the structure reveals the absorption fingerprint of the analyte and consequentially allows for identification. 100 ppm detection limit for ambient methane has been reported utilizing this technology. Integration efforts for the source and detector will further reduce the footprint and make the sensor apt for field use [93].

Flame ionization detector (FID) are widely used in benchtop GC and has now been minimized for microsystems by Kuipers et al [94]. The destructive sensor works by breaking down any hydrocarbon-containing compounds in the sample using the hydrogen flame inside the detector cavity. Ions produced in the process are then collected via a metal collector. A modified adaptation of the sensor is shown in Figure 3-6(a) [95]. In a

thermal conductivity detector (TCD), the thermal conductivity of both carrier gas and introduced analyte are compared. In the miniaturized version shown in Figure 3-6(b) the TCD is embedded into a separation column and thermal conductivity measurements are done at a reference cell at the column inlet and sample cell near the column outlet [96]. Concentration of sample is proportional to the conductivity difference. Reddy et al demonstrated the used of Fabry-Perot (FP) sensor in μGC [97]. A thin layer of vapor sensitive polymer on a substrate formed the FP detector (Figure 3-6(c)). Interference between light reflected by the air/polymer and polymer/substrate interface resulted in an interference spectrum. As the analytes entered the sensing chamber and interact with the polymer, there is a change in polymer thickness and refractive index. This leads to a spectral shift in the characteristic interference spectrum. Localized surface plasmon resonance of gold nanoparticle monolayer immobilized in a glass capillary has been demonstrated in the detection of volatile organic compounds (VOCs) with a detection limit ranging from 22 ng to 174 ng (Figure 3-6(f)) [98]. The peak width reported for the analytes were relatively broad (2.1 s – 6.1 s) even at a high flow rate of 3.5 mL/min due to dead volume created by the diameter difference between the separation column and the capillary with long detection length (10 cm). Although the sensor is compatible for μGC system, with the high value of dead volume in such a sensor it compromised the separation efficiency and is challenging for integration in a μGC system. Optofluidic ring resonator (OFRR) is another commonly used detector in μGC that combines vapor sensing and fluidic transport properties in one platform [24, 99]. A polymer coated OFRR used in conjunction with μGC system detected multiples vapor species with a detection limit at the low ppm level [100]. Later the structure was modified and coated with

nanoparticles to add detection selectivity by exploiting the wavelength dependence of VOC response (Figure 3-6(e)). This system demonstrates very narrow peaks with minimum detectable mass being 75 ng to 320 ng [101]. Combination of technologies has been useful in compensating for multiple shortcomings and optomechanical gas sensors is one of them. In a demonstration of this sensor, light in the reaction resonator undergoes a phase shift due to local refractive index change caused by the vibration of the mechanical resonator (Figure 3-6(d)). This produces a modulating output which interferes with the light in the waveguide resulting in a frequency shift in the outgoing light. Mass of gas molecules adsorbed on the mechanical resonator is proportional to this shift. Absence of coating on the mechanical resonator could lead towards a universal sensor but further analysis is yet to be done [102].

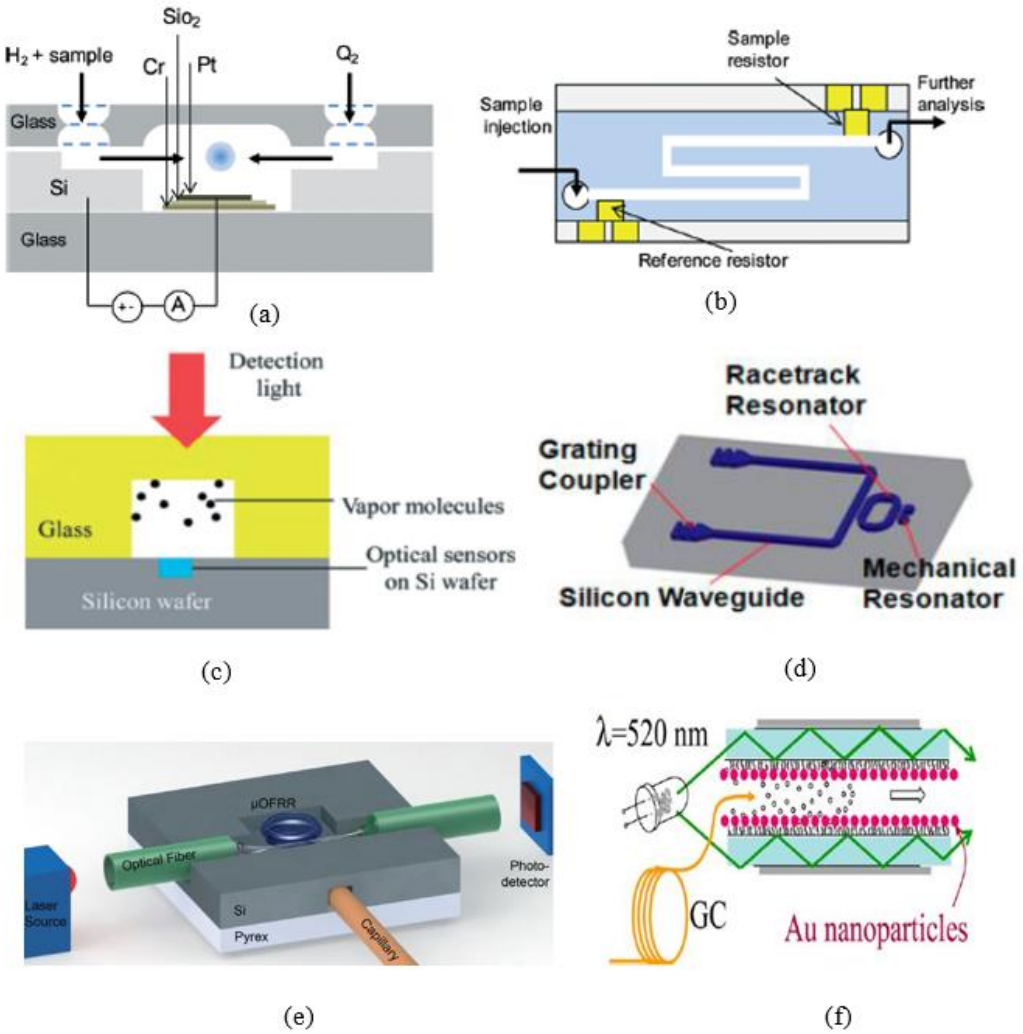

Figure 3-6 Schematic for (a) flame ionization detector [95] (b) thermal conductivity detector [96] (c)Fabry-Perot [97] (d) optomechanical sensor [102] (e) optofluidic ring resonator [101] (f) localized surface plasmon resonance [98]

Chapter 4

Characterization of micro-GC system

4.1 Introduction

The micro-gas chromatography (μGC) technology is a miniaturized version of benchtop GC system that can offer the same data reliability along with portability and ease of use. This chapter describes the assembly and characterization of the μGC system that we have developed. We have chosen either miniaturized version or fabricated the components required ourselves. It is a completely free-standing system that can be carried around in a 22”x14”x6.5” hard plastic box. The μGC system has also been used to develop methods having application in workplace safety and disease diagnosis.

4.2 System Overview

We developed a μGC system in house to analyze volatile organic compounds (VOCs) (Fig. 4-1). Its operation is segmented in three phases- sampling, waiting, and analyzing. During the sampling stage, gaseous chemicals from the sample container (canister/tedlar bag) is pulled by the vacuum pump through the 2-port valve into the preconcentrator. Preconcentrator contains adsorbents that can adsorb the chemical while it passes through it. In the analyzing stage, the preconcentrator is rapidly heated to release the chemicals as a sharp pulse of concentrated VOC mixture. The carrier gas, helium (He), then pushes the VOCs through the column where it gets separated and eventually are detected by the micro-photoionization detector (μPID) through ionization of the chemical using UV radiation. The waiting stage in between the two phases allows for the change in helium flow direction and stabilize the PID baseline. Automation of the setup and sequential implementation of the stages is done using a LabVIEW code made in

house. Additionally, a He purging step has been introduced after the test of VOCs each time to remove any chemical residues left in the µGC fluidic system.

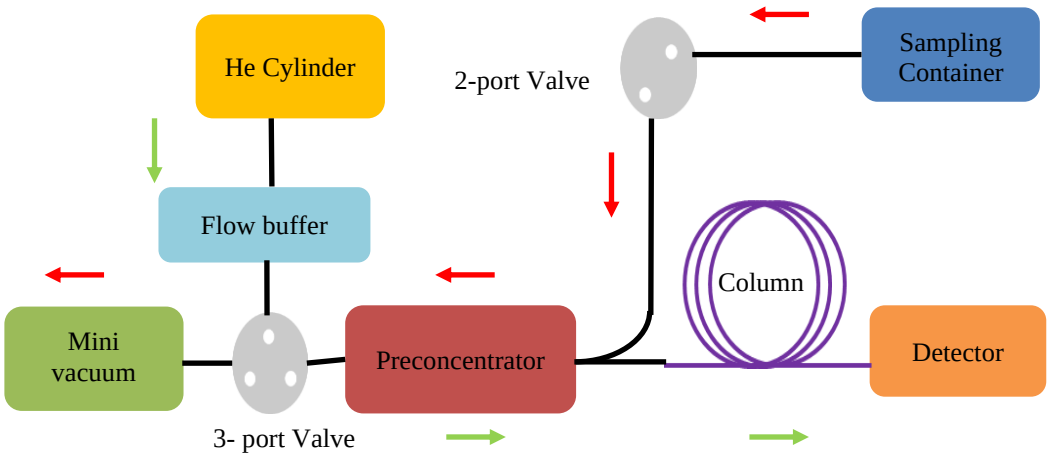

Figure 4-1 Block diagram of the µGC system. The green arrow denotes the analyzing flow stream while the red arrow denotes the sample flow stream.

4.3 Materials

Carbopack B (60-80 mesh) was purchased from Supelco (Bellefonte, PA). All the analytes used in the experiment were purchased from Sigma-Aldrich (St. Louis, MO). The chemicals had purity greater than or equal to 95% and were used as received. Rtx-5MS (5 m x 0.25 mm ID, 0.25 µm coating thickness), universal press-tight glass capillary column connectors, angled Y-connectors and guard column were purchased from Restek (Belafonte, PA). Quartz capillary (1.5 mm OD x 1.10 mm ID) were bought from Sutter Instrument Co. (Novato, CA). The 2-port and 3-port solenoid valves were purchased from Lee Company (Westbrook, CT). Silonite Canisters were bought from Entech Instruments (Simi Valley, CA). A diaphragm pump was purchased from Gast

Manufacturing (Benton Harbor, MI). Type- K thermocouple was purchased from Omega Engineering (Stamford, CT). Kanthal and nickel wires were bought from Lightning Vapes (Bradenton, FL). A data acquisition card (DAQ card), USB-6003 (16 bits) was purchased from National Instruments (Austin, TX). Customized printed circuit board (PCB) was designed and manufactured by M.A.K.S., Inc. (Troy, MI). A 36 V ac/dc converter was bought from TDK-Lambda Americas Inc. (National City, CA).12 V and 24 V dc/dc converter was purchased from CUI Inc (Tualatin, OR).

4.4 Preconcentrator

Since most real-life applications require analysis of dilute samples, we wanted to have the option to concentrate the sample before analyzing it. So, we started off with a single adsorbent preconcentrator. The construction of the preconcentrator is as shown in Figure 4-2(a). A 2.1 cm long quartz capillary with 1.10 mm ID and 1.5 mm OD is sealed at one end with silanized glass wool and then Carbopack™ B adsorbent is poured into the capillary from the other end. The open end is also sealed with glass wool. Kanthal heating wires tightly coiled on the capillary stimulate the desorption of the adsorbents. PH and PL denotes the time for which the preconcentrator is heated with the 36 V and 12 V power source respectively. At the optimized PH and PL (PH=0.3 s and PL=8 s) the recommended desorption temperature of 330 °C was obtained within 1.6 s. Figure 4-3(a) shows the chromatogram for a mixture of the 13 VOCs (Table 4-1) sampled for 2 minutes in a single adsorbent preconcentrator and separated under column temperature ramping in a 10 m column. Helium is used as the carrier gas at flow rate of 1.15 mL/min. The column was maintained at 50 °C for 1 minute and then ramped at 5 °C/min to 110

°C. All chemicals completely eluted within 7.2 minutes of release into the column. Twelve of the thirteen chemicals were separated completely however a partial overlap was observed between decane and 1,2,4-trimethylbenzene. Temperature measured by the thermocouple on the column closely follows the setpoint temperature (Figure 4-3(b)). No more than 5 °C variation is observed in the temperature profile.

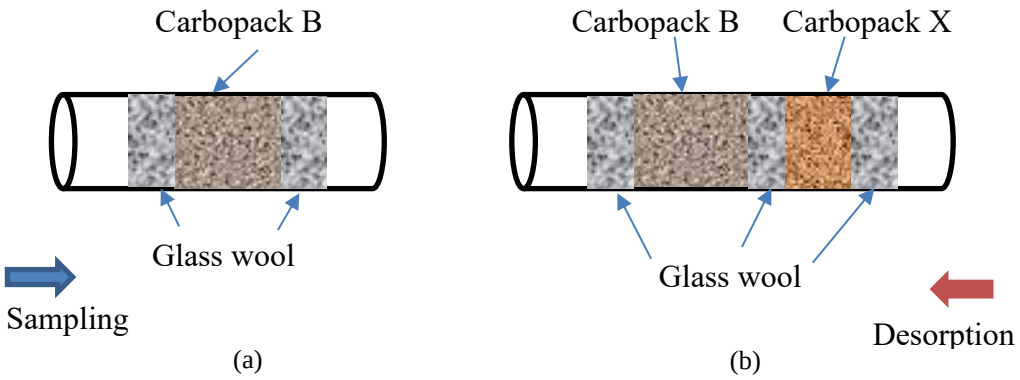

Figure 4-2 Construction of (a) single (b) dual adsorbent preconcentrator

Table 4-1 Details of the VOCs tested using the µGC system

Analyte	Peak no	Response Factor	Ionization Potential (eV)	Sampling Mass (ng)	Elution Time (s)	FWHM (s)
Isoprene	1	0.6	8.85	38.7	63.5	2.10
1-Hexene	2	NF	9.46	47.9	72.25	2.18
Methylcyclopentane	3	NF	9.85	95.7	80.25	2.39
Cyclohexane	4	1.5	9.8	95.7	89	2.61
1-Heptene	5	NF	9.34	55.8	96.25	2.31
2-methylheptane	6	NF	9.84	129.9	134.5	4.12
Hexanal	7	NF	9.72	113.9	159.75	5.00
p-xylene	8	0.5	8.45	60.4	227.25	5.67
Styrene	9	0.4	8.47	59.2	259	6.12
Heptanal	10	NF	9.65	129.9	274	11.40
Propylbenzene	11	NF	8.72	136.7	346.5	7.41
1,2,4-trimethylbenzene	12	0.43	NF	68.35	405.5	8.89
Decane	13	1.6	9.65	161.83	412	11.01

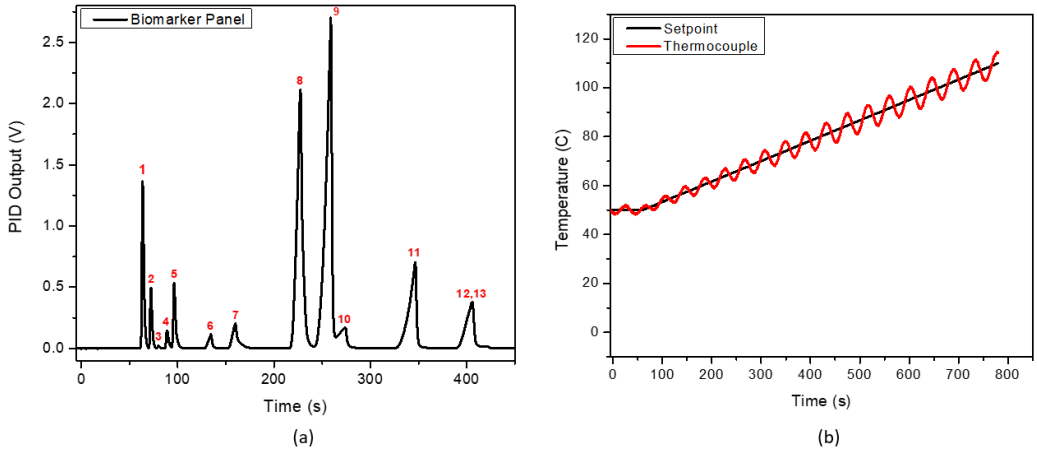

Figure 4-3 (a) Temperature programmed chromatogram for VOC mixture consisting of 13 VOC in a 10 m column with helium as carrier gas flowing at 1 mL/min with single adsorbent preconcentrator. (a) temperature profile used for separation of the mixture.

Dual adsorbent preconcentrator (Figure 4-2(b)) as the name suggests has two different kinds of adsorbents but is similar in construction. Packing multiple stages of adsorbents in correct order allows for trapping analytes with a wider range of volatility compared to a single adsorbent preconcentrator. So, to improve the preconcentrator performance a dual adsorbent preconcentrator with Carbopack B (3.2 mg) and Carbopack X (1.9 mg) packed in a quartz capillary with the same dimension was fabricated. Carbopack X is suitable for analyte size relative to C_3-C_9 alkanes while Carbopack B is more appropriate for C_5-C_{12} alkanes. Generally, the higher the surface area of an adsorbent the higher would be its adsorption strength. The surface area for Carbopack B and Carbopack X are 100 m^2/g and 240 m^2/g respectively. Adsorbents with large surface area are used to trap compounds with high volatility. These large surface area adsorbents

are usually placed downstream in the sampling gas flow path so that the low volatility compounds will not be trapped in these adsorbents. So out of the two adsorbents chosen Carbopack X is placed latter in the sampling path. The temperature profile for different heating time was characterized in Figure 4-4(a) to make sure that the recommended desorption temperature of 330 °C is reached within a short time. For this measurement, a thermocouple probe is inserted into the unloaded capillary and made sure that it lies right beneath the coil. Then the temperature for different heating (PH and PL) parameters on the code is recorded. Both the preconcentrators were thermally conditioned to ensure that the adsorbents were free of any kind of chemical residue before testing. They were conditioned at 330 °C for 12 hours with constant helium flow of 1.24 mL/min.

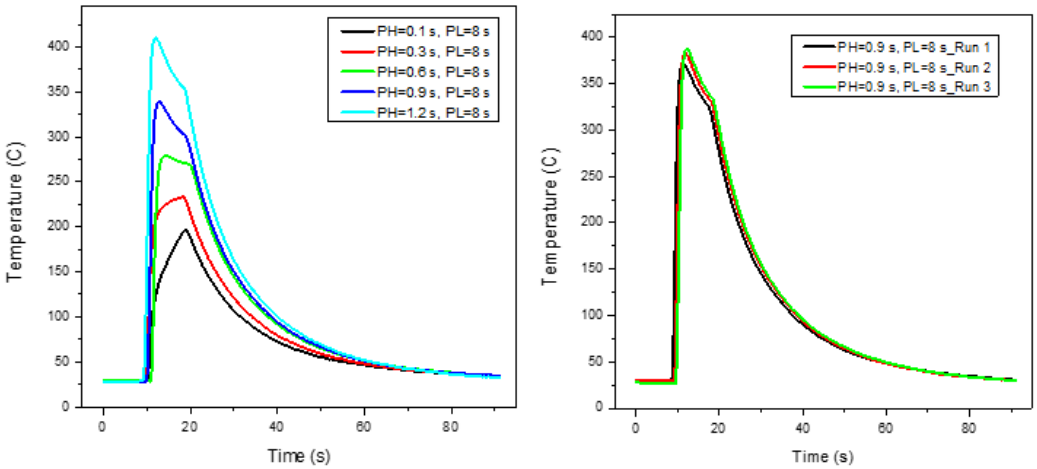

Figure 4-4 (a) Relationship between heating parameters and the temperature profile obtained inside a quartz capillary used to make the dual adsorbent preconcentrator. (b) Repeatability of the temperature profile. ID and OD of the capillary are 1.10 mm and 1.5 mm, respectively.

Out of all the PH and PL parameters tested (Figure 4-4(a)) PH=0.9 s and PL=8 s was chosen for the chemical testing as it allows the temperature to reach the recommended desorption temperature of degree 330° C within 1.49 s and keeps the maximum temperature below 400° C. The other parameters either does not reach 330° C or goes above 400° C quite fast. Previous experiment shows that the temperatures measured in an empty preconcentrator and loaded one are very similar. So, the measured temperature in this method can be considered to be what the adsorbents would be experiencing inside the preconcentrator. Figure 4-4(b) shows the repeatability of the temperature profile for the chosen PH and PL parameters.

4.5 Micro Photoionization Detector (µPID)

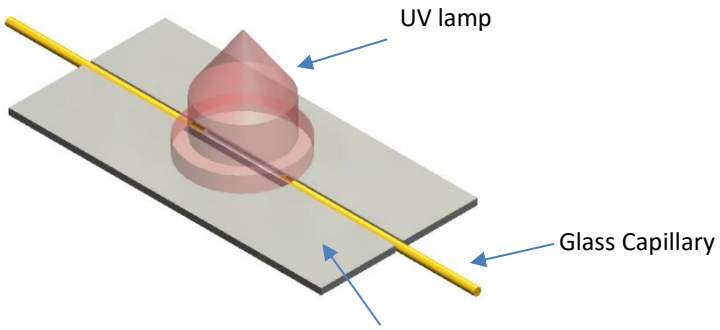

Figure 4-5 Schematic of µPID

Photoionization detectors (PID) can detect VOCs by ionizing them on exposure of UV light. The ionized electrons are then collected by a set of electrodes with voltage applied across them. The intensity of current generated by the electrons depend on a number of factors- vacuum ultraviolet (VUV) photon flux, effective VUV radiation are of

an ionization chamber, ionization cross section, analyte concentration and ion/electron collection efficiency at electrodes. The response time of the detector is determined by the time required by the analyte to flow through the ionization chamber and the time required to purge out the analyte left in the dead volume. So both the ionization volume and dead volume regulates the time response of the sensor [103]. We fabricated a µGC by modifying the ionization chamber of a commercially available PID. The UV lamp of the commercial PID was removed from its housing and glued on a glass channel with conductive silicon wafer as channel wall. The channel was sealed with optical glue and guard columns served as inlet and outlet of the channel as shown in Figure 4-5. The lamp drive circuit and signal amplifier from the commercial circuit was used to make the system functional.

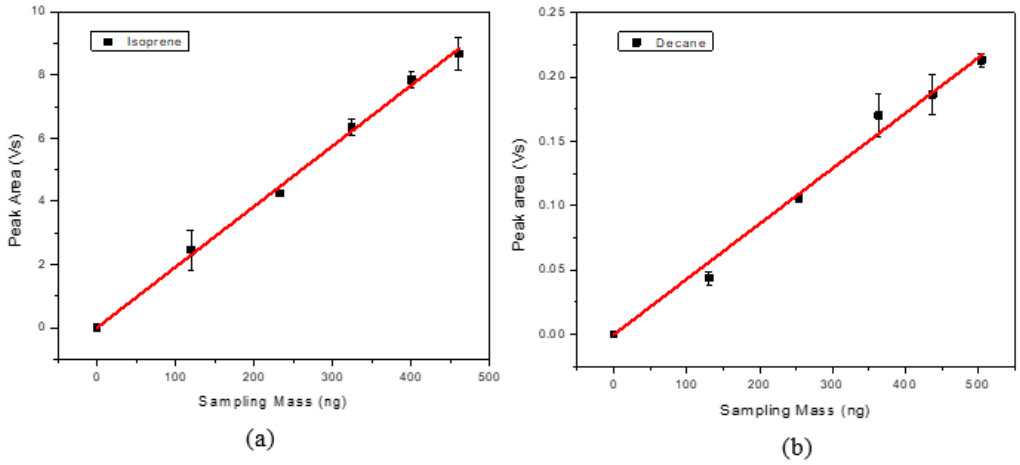

Figure 4-6 Calibration curve for analytes in the µGC setup with a 10 m column and He at 2 mL/min (a) isoprene (b) decane

Figure 4-6 shows the calibration curve for the most (isoprene) and the least (decane) volatile chemical in the list. For calibration a known volume of the liquid

chemical is injected into a 6 L canister under vacuum and then diluted with helium. The chemicals were calibrated with helium carrier gas flowing at 2 mL/min while the column is held at 30 °C for 1 min and then ramped at 30 °C/min to 120 °C and stalled for 1 min at the highest temperature. Both the chemicals show linear relationship between peak area and sampling mass. Decane exhibit a sensitivity of 0.43 mVs/ng while isoprene has a sensitivity of 19.2 mVs/ng. One of the key factors determining sensitivity of any chemical is ionization factor. The lower the ionization potential of a chemical the more probable it is to be ionized and hence a better PID response is expected for it. Ionization potential for isoprene (8.85 eV) is smaller compared to that of decane (9.65 eV) making the µPID more sensitive to isoprene**.** The rest of the chemical in the biomarker panel show similar trend.

4.6 Separation Column

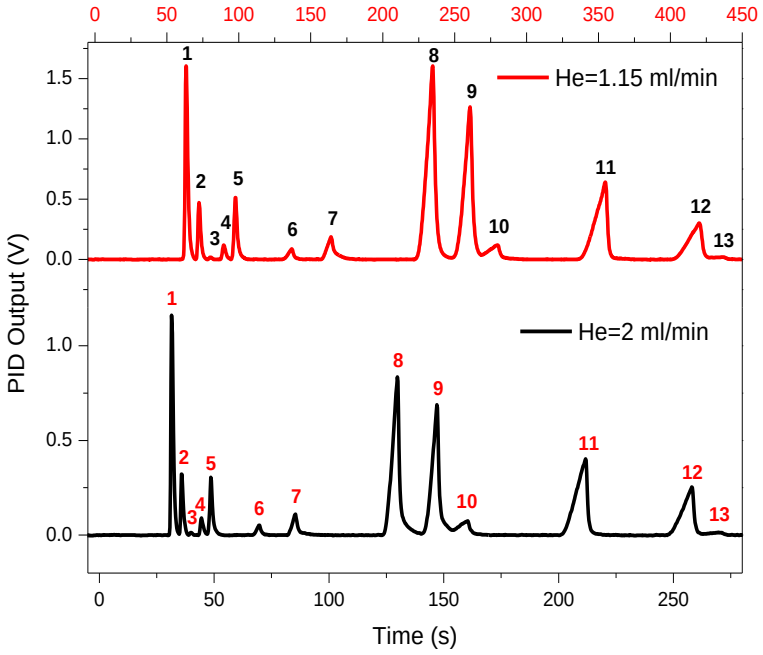

Figure 4-7 Effect of carrier flow rate on biomarker panel separation. The mixture analytes are shown in Table 4-2 with their corresponding peak no.

We used a 10 m Rtx-5ms column in the µGC setup to serve the purpose of separation of analytes. To ameliorate peak broadening issue, we increased the carrier flow rate as shown in Figure 4-7. from 1.15 mL/min to 2 mL/min. Preconcentrator used on the setup is made of quartz capillary having 1.10 mm ID and 1.5 mm ID. It is packed with 3.3 mg of Carbopack B and heated using a kanthal wire coiled on the outside. The LabVIEW code was modified to allow for a two-step ramping in column heating. With the modified temperature profile, the column temperature is held at 50° C for 1 min and then ramped at 5 °C/min to 120 °C and held there for 1 min. This also allowed for the elution temperature of the analytes to increase. Higher flow rate reduced the peak width as well as the fronting issue to some extent. The decane peak is also more visible but it is still partially overlapping with the adjacent peak. Increase in the flow rate also allowed for shorter analysis time. Table 4-2 shows the comparison in peak width of the biomarker analytes for different flow rates of the carrier gas used in the setup.

Table 4-2 Comparison in peak width for different flow rates with a single adsorbent preconcentrator in the µGC setup.

Analyte	**Peak No**	**Mass (ng)**	**FWHM (s)**	
			He=1.15 mL/min	**He=2 mL/min**
Isoprene	1	38.7	2.05	1.07
1-Hexene	2	47.9	2.09	1.19
Methylcyclopentane	3	95.7	2.32	1.19
Cyclohexane	4	95.7	2.50	1.32
1-Heptene	5	55.8	2.30	1.20
2-methylheptane	6	129.9	3.83	1.95
Hexanal	7	113.9	4.60	2.30
p-xylene	8	39.9	5.91	3.09
Styrene	9	42.6	5.81	3.07
Heptanal	10	129.9	8.51	5.75
Propylbenzene	11	136.7	8.87	5.47
1,2,4-trimethylbenzene	12	68.4	10.03	5.33
Decane	13	161.8	8.63	7.34

4.7 Lung Cancer Biomarker analysis in µGC

Following past year trends Lung Cancer (LC) continues to be a global health concern. According to American Cancer society United States is expected to have 235,760 new patients and 12% male and 22% female of the total deaths is projected to be caused by Lung Cancer making it the leading cause of cancer death in 2021 [104]. It is often identified at an advanced stage by clinical methods like biopsy of lung nodules, bronchoscopy, or computed tomography (CT) imaging when death can be hardly avoided. In addition to that these processes are also quite time consuming, costly and painful or stressful. The urgent need of a fast, inexpensive and noninvasive diagnostic tool paved the path towards this application of µGC system.

In 1971 Linus Pauling first introduced us to the chemical content of human breath sample by detecting 250 VOCs using temperature-programmed gas-liquid partition chromatography [105]. Suggesting a possible application Phillips et al compared breath sample from patients with and without lung cancer using Gas chromatography-Mass Spectroscopy (GC-MS) [106]. Afterwards, solid phase microextraction (SPME) in combination with GC used by Chen et al [107] established the correlation between metabolic products of lung cancer cells and volatile organic compounds present in breath sample of lung cancer patients. This research served as the biological basis to use breath analysis in detection of lung cancer. Literature review shows different sensing mechanism coupled with gas chromatography for breath analysis of lung cancer patients. Some noteworthy works were done using carbon nanotubes[108], quartz microbalance (QMB) sensor [109] and surface acoustic wave sensors[110].

The μGC technology that we have developed is simple, noninvasive, inexpensive, and fast and thus has the advantage of being patient friendly and potentially not requiring highly trained staff to operate. Despite of its pros it cannot be regarded as a stand-alone identification method due to lack of standardization between different method and absence of a group of clinically certified biomarkers for the detection of lung cancer. However, it can always be used as a preliminary inexpensive and quick indicator which can be further verified by the traditional methods.

Breath is a complex mixture of numerous VOCs. Some of them has endogenous origin while other are contributed by the environment. Researchers have used various combination of endogenous VOCs to distinguish between LC patients and healthy controls [106, 107, 111-120]. Out of these, 15 VOCs have been selected for investigation in our studies. Table 4-3 shows the concentration range at which an analyte has been reported in people with lung cancer and healthy people. Numerical values for concentration could not be found for two of the chemicals, 2-methylheptane and 1-Heptene but they have been used as a distinguishing LC biomarker in literature [106].

Table 4-3 Concentration of the VOCs in exhaled breath of healthy volunteers and Lung cancer (LC) patients

Analyte	Healthy volunteer		LC patient		Reference
	ppb	ng/ml	ppb	ng/ml	
Isoprene	3.76-184		2.88-202		[107, 111, 112]
Acetone	627.5		458.7		[111, 112]
Methanol	142.0		118.5		[111]
1-Hexene				>0.2628	[107]
Methylcyclopentane				>1.7264	[107]
Benzene				>0.05122	[107, 112, 113]
Undecane		0.15 ng/ml		0.10-8.51	[107, 113]
Cyclohexane	0.00–0.48		0.00–1.71		[112]
Ethanol	0-68.7		0-160		[112]
Hexane	0-4.82		0-6.28		[112]
Toluene	0-1.13		0-1.82		[112]
Octane	0-3.66		0-3.38		[112]
Nonane	0-1.35		0-18		[112]
Phenyl acetate	0.01-4.27		0-7.53		[112]
Acetoin		1.29×10^{-3}		8.28×10^{-3}	[114]
1-Butanol		2.18×10^{-3}		6.36×10^{-3}	[114]
1-Heptene					
Pentane		8.3×10^{-4}		1.73×10^{-3}	[115]
O-Toluidine		$(9.05\text{-}246) \times 10^{-6}$		$(7.65\text{-}97.25) \times 10^{-5}$	[116]
Heptane	0-6.26		0-7.36		[112, 117]
2-methylheptane					
Hexanal				>0.02272	[107, 118]
Ethylbenzene	8.6-14.0		4.6-89.3		[112, 119]
p-xylene	4.5 – 58.9		1.6 – 32.7		[119]
Styrene				>0.15032	[107, 113, 117]
Heptanal				>0.05188	[107, 118]
Propylbenzene				>0.11908	[107, 113]
1,2,4-trimethylbenzene				>0.02298	[107]
Decane	0.26-18.5		0.06-62.9		[107, 112, 113]

4.7.1 Synthetic LC Biomarker Method Development

Researchers have investigated a variety of biomarkers for the detection of lung cancer. To increase the probability of detecting true positive and optimize the performance of the μGC system some more VOCs were added into the panel. The temperature profile and the injection mass were also optimized to ameliorate the separation performance of the setup. Figure 4-8(a) shows the chromatogram for the chosen biomarker panel. They were sampled for 8 minutes and separated under column temperature ramping in a 10 m column. Helium is used as the carrier gas at flow rate of 2 mL/min. The column was maintained at 30 °C for 1 minute and then ramped at 5 °C/min to 33 °C and then ramped again to 120 °C at 30 °C/min and held there for 2 minutes. All the chemicals completely eluted within 5 minutes of release into the column and were separated completely. According to Table 4-4 peak width for the highly volatile VOCs (isoprene to heptane) were less than 2 s. The broadest peak width was observed for decane (~5 s). The optimized temperature profile allowed for higher column temperature when the least volatile compounds elute thus reducing the peak width. The peak area of the chemicals closely follows the trend in their ionization potential. The lower the ionization potential of a chemical the more probable it is to be ionized and hence a better PID response is expected for it. The temperature ramping profile is presented in Figure 4-8(b). Temperature measured by the thermocouple on the column closely follows the setpoint temperature. No more than 8 °C variation is observed in the temperature profile. The improved system configuration allows for compete separation of the biomarkers in reduced time.

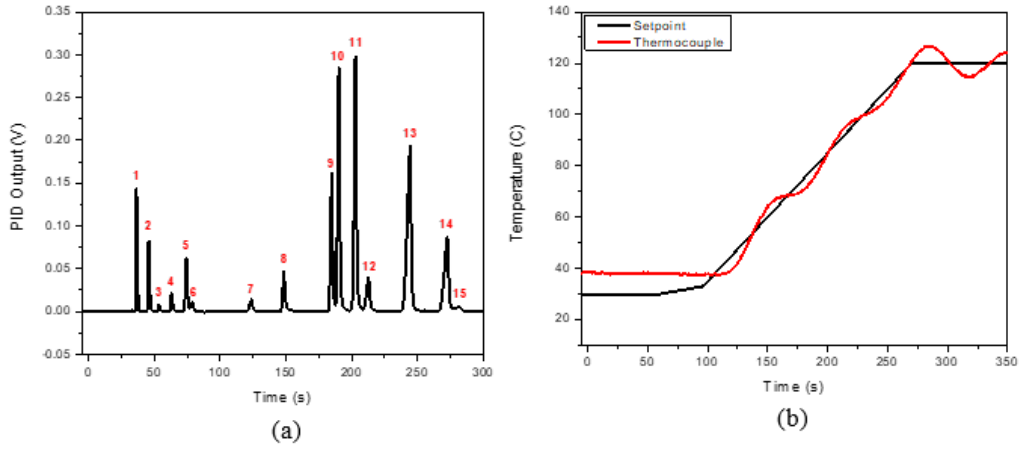

Figure 4-8 (a) Temperature programmed chromatogram for the biomarker panel consisting of 15 VOC in a 10 m column with helium as carrier gas flowing at 2 mL/min. (b) Temperature profile used for separation of the biomarker panel. Details of the peaks are provided in Table 3

Table 4-4 Details of the VOCs tested in the µGC system

Analyte	Peak No	Concentration in Canister (ng/L)	Sampling Mass (ng)	Elution Time (s)	FWHM (s)
Isoprene	1	357.4	14.3	36.5	1.06
1-Hexene	2	841.0	33.6	45.7	1.22
Methylcyclopentane	3	3216.1	128.6	53.6	1.39
Cyclohexane	4	966.3	38.7	63.2	1.44
1-Heptene	5	864.6	34.6	74.3	1.6
Heptane	6	2595.4	103.8	78.9	1.94
2-methylheptane	7	1332.1	53.3	123.4	2.44
Hexanal	8	1009.7	40.4	148.5	1.76
Ethylbenzene	9	413.6	16.5	184.8	1.61
p-xylene	10	575.1	23.0	190.3	1.54
Styrene	11	605.2	24.2	202.9	1.71
Heptanal	12	1559.2	62.4	212.8	2.74
Propylbenzene	13	1645.0	65.8	244.4	3.24
1,2,4-trimethylbenzene	14	1091.6	43.7	272.5	3.51
Decane	15	1915.6	76.6	282.0	5.12

4.7.2 Human Breath Analysis in µGC system

Figure 4-9 shows the chromatogram for the breath sample tested in the µGC system for different sampling time with inhalation through both mouth and nose. Breath sampling was done in a Tedlar bag as mentioned in the previous section. The breathing line was constructed using medical grade PTFE connectors and mouthpiece along with moisture filter to reduce the possibility of VOC adsorption to and release from the connectors or the mouthpiece. The breath components were separated by a 10 m Rtx-5ms column held at 30 °C for 1 min, ramped to 33 °C at 5 °C/min and further ramped to 120 °C at 30 °C/min and held there for 2 min. Helium was flown through the column at 2 mL/min. Since µPID is unable to determine the chemical structure of the VOC although some chemicals were detected in this setup, but we could not identify them. Also, most of the peaks detected were too small to be regarded as an actual chemical. The inset in Figure 4-10 attempts to give a closer look at the smaller peaks. The intensity of the significant peaks increased with the sampling time although the smaller peaks seem to be less affected by the sampling time. Inhalation through nose or mouth hardly affected the intensity of the chemical peaks.

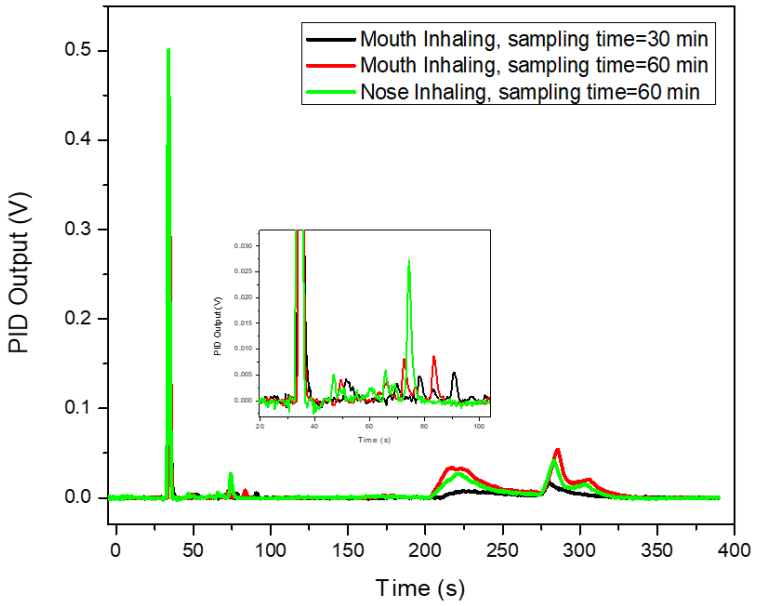

Figure 4-9 Temperature programmed chromatogram of healthy human breath sample in µGC system with new breathing line configuration and inhalation through mouth and nose

4.7.3 Integration of µGC system with Mass Spectrometer (MS)

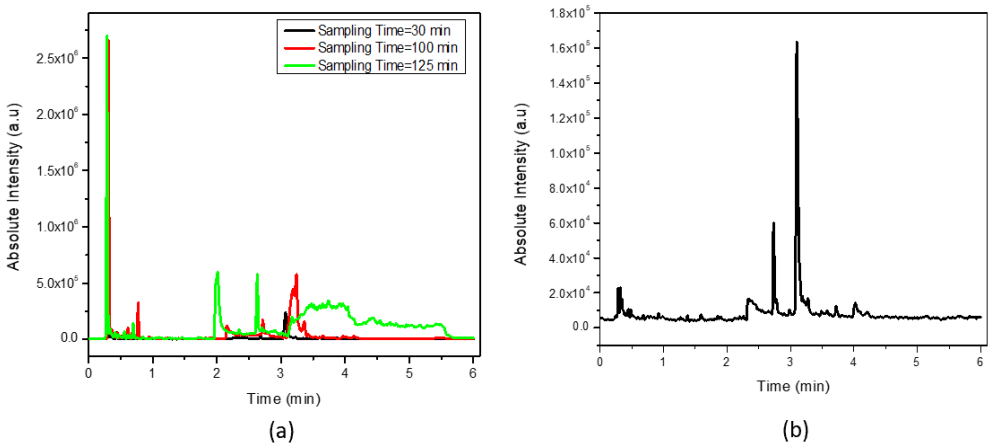

Figure 4-10 Temperature programmed chromatogram for (a) healthy human breath sample (Subject 01) (b) Helium collected in a tedlar bag through the breathing line, sampled and separated by µGC and then detected by a single quad mass spectrometer for different sampling time.

Figure 4-10(a) shows the chromatogram obtained using the μGC-MS system for the breath sample of subject 01 for different sampling time. It is observed that the peak intensity increases and, in some cases, also broadens as the sampling time is increased. This indicates that the preconcentrator has enough sample capacity to trap the VOCs from the breath sample. The highest number of chemicals having greater than 90% probability with respect to the GC-MS library was for sampling time of 100 min. The probable chemical identity of this breath sample is listed in table 4-5. Researchers have also reported finding isoprene, p-xylene and nonanal in breath sample before [107, 119, 121]. The other samples from the same subject having different sampling time had similar composition. Isoprene is observed in the breath signals for all sampling times having very high signal intensity. To rule out the probability of the chemicals to be coming from the Tedlar bag or the breathing line the Tedlar bag is filled with helium through the breathing line. Basically, the breath collection process is repeated while replacing the breath sample with helium. Figure 4-10(b) suggests that none of the chemicals predicted to be contributed by breath was found in this control experiment.

Table 4-5 Probable identity of the analytes in breath sample of subject 01 for a sampling time of 100 min

Retention Time (min)	Probable compound	Probable source
0.31	Isoprene	breath
0.37	Silanol	bag/setup
0.46	Tetrahydrofuran	bag/setup
0.68	2-butanethiol	breath
0.95	Toluene	bag/setup
1.92	p-xylene	breath
2.16	N,N-dimethylacetamide	bag
2.72	Benzaldehyde	setup
3.24	Phenol	bag
3.65	Acetophenone	bag/setup
3.96	Methyl ester Benzoic acid	bag/setup
4.14	Nonanal	breath

4.8 Method development for workplace hazardous VOCs

We used 17 analytes listed by different research work as a common danger to people working in different industries and attempted to analyze then using the μGC system. Sub-ppm concentration of analyte was separated using a 10 m column with carrier flow rate of 2 mL/min (Figure 4-11). The column was set at 30 °C for 0.5 min and then ramped to 50 °C at 30 °C/min and held there for 2.5 min. The temperature was then again ramped to 130 °C at 50 °C/min and held there for 1 min. Separation of all the analytes was achieved in less than 6 min. However, there were two sets of partial coelution one between analyte 5,6,7 and 8 and the other one between 12 and 13. But the intensity of the coeluted peaks were such that they could still be identified. Details of the separation is provided in Table 4-6.

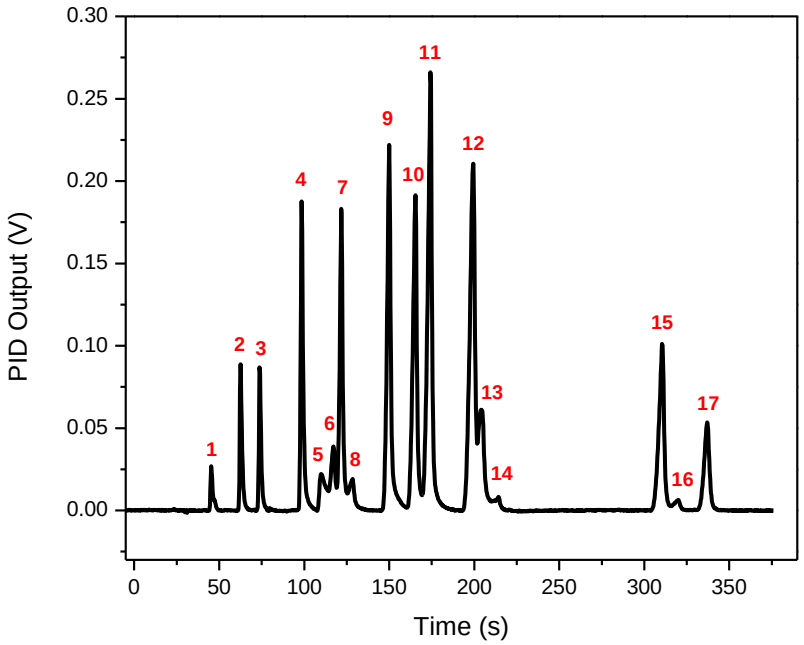

Figure 4-11 Temperature programmed chromatogram for 17 workplace hazardous VOCs separated using 10 m column with 1.78 mL/min carrier flow rate.

Table 4-6 Details of the workplace hazardous VOCs tested in the µGC system

Analyte	Peak No	Elution Time (s)	FWHM (s)	Concentration (ppm)
Vinyl Acetate	1	44.3	1.32	0.31
Benzene	2	61.3	1.35	0.17
Trichloroethylene	3	72.5	1.26	0.16
Toluene	4	96.8	1.47	0.14
Dimethylformamide	5	108	5.21	0.37
Hexanal	6	114.3	2.92	0.29
Tetrachloroethylene	7	119	1.83	0.28
Chlorobenzene	8	125.3	4.22	0.37
Ethylbenzene	9	146.3	2.17	0.28
m-xylene	10	161.3	2.50	0.23
Styrene	11	169.3	2.52	0.23
2-heptanone	12	194	3.24	0.25
n-Nonane	13	201.8	4.18	0.20
1,2,4 Trimethylbenzene	14	209.3	6.13	0.16
n-Decane	15	305	3.17	0.21
R-Limonene	16	316	4.88	0.25
Chlorobenzene	17	332.3	3.35	0.35

Chapter 5

Integration of 2D Photonic Crystal Slab Sensors with micro Gas Chromatography

5.1 Introduction

Micro-gas chromatography (μGC) systems have shown immense growth in the last two decades [90, 95, 122-125]. It provides a less invasive option in gas analysis that can be monitored in real time and offer reliable quantitative data in essential sectors like industry, healthcare, environment, and national security. The key attributes of a μGC system is compact, automatic, reduced power consumption, minimal maintenance costs, and suitable for field analysis. Thus, it provides the advantages of rapid analysis and turnaround time as well as simpler sample preparation. The miniaturization of a GC system called for miniaturization of the detectors as well. Conventional detectors suffer from large dead volume and thus slow response time. Out of various transduction mechanisms used in μGC systems so far, optical sensing has emerged to be a popular mode of sensing due to its immunity to electromagnetic interference and cross talk, high sensitivity, ability to function in hazardous conditions, remote operation, and fast response. Some optical detectors used in μGC are based on surface plasmon resonance [98], ring resonator [24, 99], Fabry-Perot interferometry [97], diode laser spectroscopy [126], optomechanical sensor [102], and photoacoustic spectroscopy [127]. Although all these works have reported reasonably moderate sensing performance in conjunction with GC platform, they either have large dead volume, are tough to reliably fabricate on large scale or have a complicated optical design.

Photonic crystals (PC) have adopted the inherent properties of optical sensors along with compatibility to standard silicon IC fabrication for reliable mass production and on chip integration. Its strong optical confinement capability and compact orientation makes it even more attractive in sensing applications [52, 128, 129]. The strong light-matter interaction in photonic crystal slab (PCS) sensor allows for detection of dilute samples within a small interaction volume. Flat photonic bandgap and low group velocity of light in the periodic structure provides for large interaction time. Lower group velocity of light in photonic crystal also gives higher enhancement factor. These structure with defects (point or line) allows for even better light localization. 2D defect-based PC has been broadly explored for gas sensing in mainly two forms, PC cavity and PC waveguide [130-133]. Although high sensitivity and good Q-factor were demonstrated in most of the PC based gas sensing, PC inherently lack detection specificity. The selectivity issue can be solved by using PCS sensors together with a μGC. A mixture of gases flowing through a GC column separates from each other, resulting in individual analytes arrive at the end of the column at a unique time (i.e., elution time). The real time response from a micro-detector placed at the end of the column can identify analytes specifically through the elution time and quantitatively through the signal intensity to reveal the analyte concentration. An ideal microsensor for μGC should have negligible dead volume, efficient gas fluidics, and fast intrinsic response time, so that the detector induced peak broadening is minimal, thus maintaining the separation resolution of the μGC system. Additionally, high sensitivity is desirable to enable trace vapor analysis.

Here, we have described the integration of a μGC with a 2D defect free PCS sensor through transfer printing process and its application in separation and detection of

complex VOC mixtures. To the best of our knowledge this is the first work on integration of photonic crystal sensors with μGC. An easy to implement cross polarization optical setup is used to couple the Fano resonance of a defect free PCS in free space. We first developed and assembled a portable μGC system that is fully automated using a LabVIEW program. Si PCS fabricated on SOI substrate was transfer printed using PDMS stamp onto glass substrate and then anodically bonded to a silicon microfluidic channel which has a similar dimension to the μGC column to integrate with the μGC system without compromising efficient gas fluidics. The integrated system was used to separate and detect a mixture of 10 VOCs in under 4.5 min. Transfer of the PCS on a glass wafer makes it also compatible to the microfabricated Si GC columns. Separation and detection of 4 VOC mixture was demonstrated using an integrated Si μGC column and on-column PCS sensor at room temperature.

5.2 Materials and Methods

5.2.1 Materials

Carbopack B (60-80 mesh) and Carbopack X (40-60 mesh) was purchased from Supelco (Bellefonte, PA). Analytical grade pentane, hexane, heptane, benzene, trichloroethylene, toluene, hexanal, chlorobenzene, ethylbenzene, p-xylene and 2-heptanone were purchased from Sigma-Aldrich (St. Louis, MO). The chemicals had purity greater than or equal to 99% and were used without any further modification. OV-101 was acquired from Ohio Valley Speciality Company (Marietta, OH). Rtx-5MS (10 m x 0.25 mm ID, 0.25 μm coating thickness), universal press-tight glass capillary column connectors, angled Y-connectors, tedlar bags, and guard column were purchased from Restek Corporation (Belafonte, PA). Quartz capillary (1.5 mm OD x 1.1 mm ID) were

bought from Sutter Instrument Co. (Novato, CA). The 2-port and 3-port solenoid valves were purchased from Lee Company (Westbrook, CT). A diaphragm pump was purchased from Gast Manufacturing (Benton Harbour, MI). Type-K thermocouple was purchased from Omega Engineering (Stamford, CT). Kanthal and nickel wires were bought from Lightning Vapes (Bradenton, FL). A data acquisition card (DAQ card), USB-6003 (16 bits) was purchased from National Instruments (Austin, TX). Silicon wafers were acquired from University Wafer Inc (South Boston, MA). Customized printed circuit board (PCB) was designed and manufactured by M.A.K.S., Inc. (Troy, MI). A 36 V AC/DC converter was bought from TDK-Lambda Americas Inc. (National City, CA). 12 V and 24 V DC/DC converter was purchased from CUI Inc (Tualatin, OR). Miniature helium cartridge was purchased from Leland Gas Tech (South Plainfield, NJ). All optical components were procured from Thorlabs (Newton, NJ) and Edmund Optics (Barrington, NJ).

5.2.2 Sample Preparation

To evaluate the integration of the μGC system with the PCS sensor 11 polar and non-polar VOCs were used. Heptane along with 3 other VOCs from this list was used to show isothermal separation and detection using the Si μGC column and on-column PCS detector. The chemical and physical properties of the chemicals are summarized in Table 5-1 [134-138]. The mixture is formulated by mixing equal volume of all the analytes in their liquid form. A certain volume of the liquid mixture is then injected into a 3L tedlar bag filled with helium using a gas tight syringe. The injected liquid vaporized in the bag and form the test vapor. To prepare a sample of concentration below 10 μg/L, the analytes were first

dissolved in pentane and then injected into the tedlar bag. For high concentration sample (above 40 µg/L), the required volume of the analyte was injected into the tedlar bag directly.

Table 5-1 Characteristics of the analytes at room temperature

Chemical Name	Vapor Pressure (Torr)	Partition Coefficient	Polarity
Pentane	434	82	Nonpolar
Hexane	132	215	Nonpolar
Heptane	53.3	565	Nonpolar
Benzene	95	296	Nonpolar
Trichloroethylene	47	981	Polar
Toluene	28.5	815	Nonpolar
Hexanal	10	2300	Polar
Chlorobenzene	11.8	2494	Polar
Ethylbenzene	10	2020	Nonpolar
p-xylene	9	2220	Nonpolar
2- Heptanone	3.9	3617	Polar

5.2.3. Fabrication and assembly of µGC

The µGC system is assembled using miniatured components most of which are sourced off the shelf with the exception of preconcentrator which was fabricated in house. All the components are electrically connected to custom designed PCB board and controlled using a homemade LabVIEW program. Figure 5-1 shows the schematic of the µGC system, which is a completely free-standing system that can be carried around in a 22”x14”x6.5” hard plastic box. Sampling is carried out by the mini vacuum pump that pulls the analytes from the tedlar bag through the preconcentrator allowing them to get accumulated there. After a period of helium flow through the preconcentrator to remove any VOCs that failed to get adsorbed, the analyzing phase starts. At the start of this phase, the preconcentrator is heated using a combination of 36 V and 12 V power source to reach 330 °C in less than 1.7 s to release a sharp peak of analyte mixture that is

injected into the column by the carrier gas helium. The preconcentrator is constructed using a 3.3 cm long quartz capillary with 1.5 mm OD and 1.10 mm ID. Carbopack B and Carbopack X are used in sequence in the sampling path to trap analytes with vapor pressure ranging from 0.01 Torr to 95 Torr [139]. The tube is heated through resistive heating by tightly wrapping Kanthal wire around the tube. For all measurements helium flow rate of 1 mL/min was used. 10 m of Rtx-5ms column was employed for all temperature programmed separation while a 3m OV-101 coated on the microfabricated silicon μGC column was used for room temperature separation. The analytes are injected into the μGC system at room temperature from a 3 L tedlar bag using the vacuum pump within 4 min. The column temperature was initially set at 30 °C and then ramped at 30 °C/min to 90 °C. It was held at the final temperature for another 2 min. After separation, the analytes are detected using a 2D PCS free space coupled sensor, which was connected to the GC column by a 10 cm guard column. The optical setup used for detection has been described in detail in our previous publications [37, 39]. Briefly, a tunable laser source was focused on the PCS sample through a collimator, linear polarizer, and lens under surface normal incidence condition. A beam splitter at the end of this optical path splits the reflected light and allowed it to pass through another polarizer and finally to a photodiode. The reflection spectrum of the PCS was collected through a cross polarization setup to reveal the symmetry-protected bound states in the continuum modes that are used for sensing [39, 140].

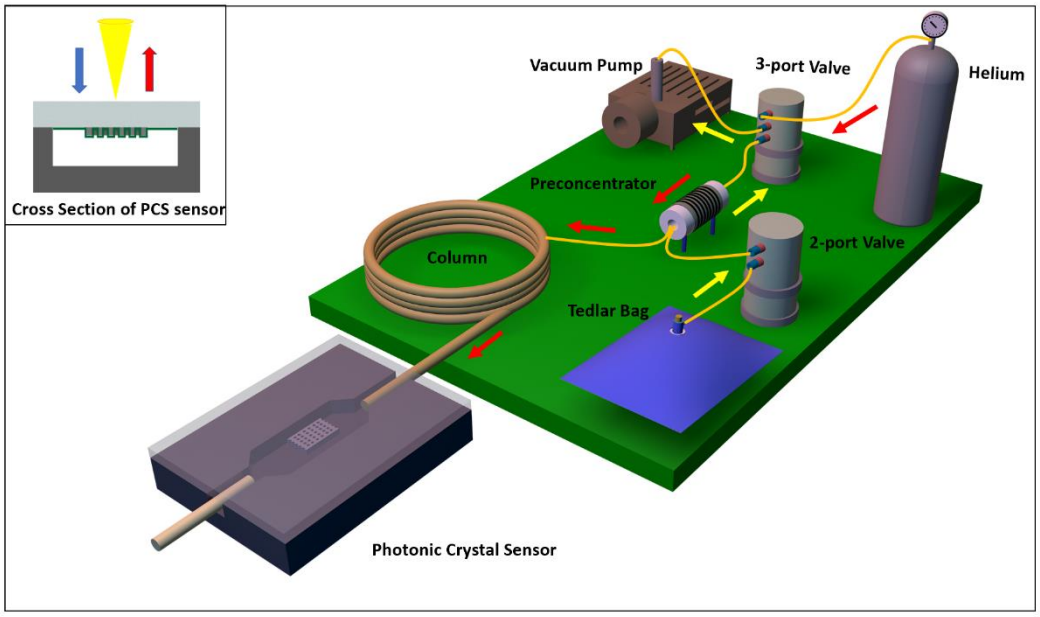

Figure 5-1 Schematic of integrated µGC-PCS gas analysis system. The portable µGC system is packed into a small briefcase. The operation of µGC is controlled by a homemade LabVIEW code. Yellow (red) arrow shows the flow direction during the sampling (analyzing) stage. Inset shows the cross-section view of the PCS sensor in a microfluidic channel.

5.3 Results

5.3.1. PCS sensor design, fabrication, and characterization

Si PCS Fano resonance optical filter was first fabricated on a silicon-on-insulator (SOI) substrate using e-beam lithography (EBL) and reactive-ion etching (RIE) [141]**.** Si PCS with lattice constant, a=976 nm, air hole radius, r=75 nm, Si slab thickness, t=240 nm and a buried oxide layer of 3 µm leads to a center wavelength of Fano resonance around 1500 nm. Refractive index (RI) for Si, OV-101 polymer and SiO_2 is 3.48, 1.4 and 1.45, respectively. SEM image of the PCS on SOI is presented in Figure 5-2 (a,b).

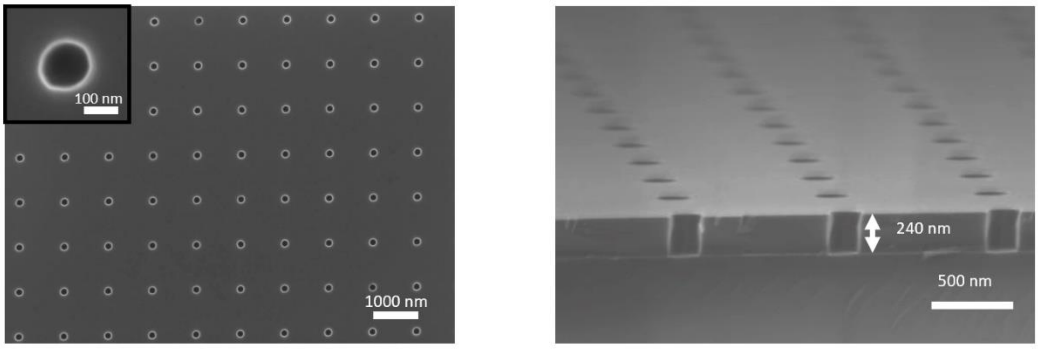

Figure 5-2 SEM image of the PC sensor on SOI substrate with a= 976 nm, r=75 nm, t=240 nm before transfer (a)Top view, inset shows the top view for a single air hole in the PC (b) Cross sectional view

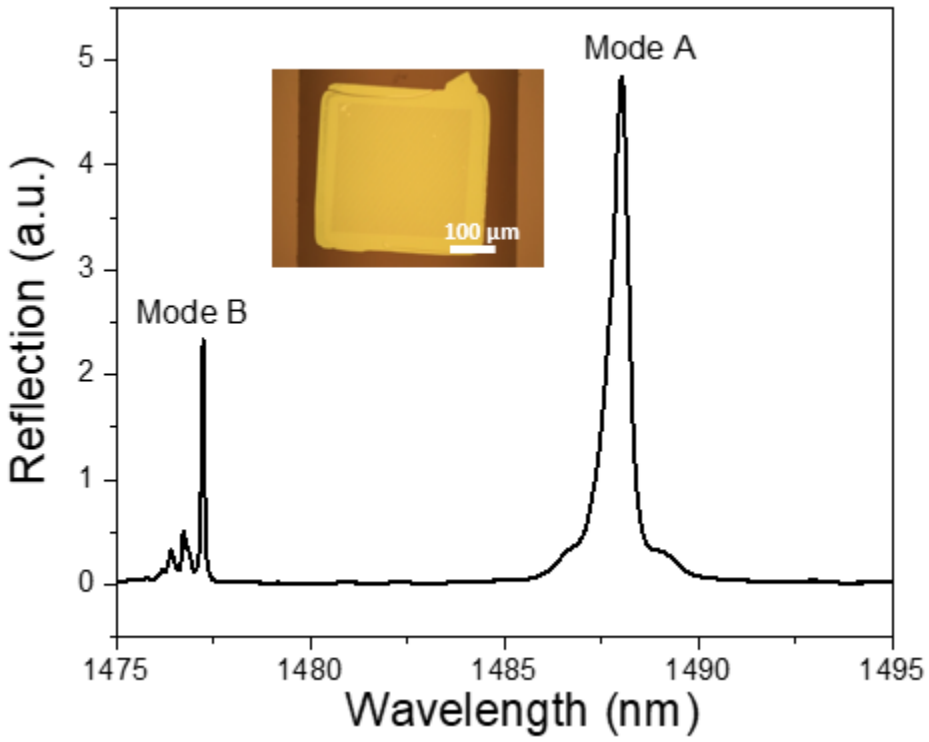

Figure 5-3 Measured reflection spectra of the PCS sensor on glass substrate after transfer. Inset shows a microscope image of the PCS after transfer in a microfluidic channel.

Transfer Printing is then used to transfer the PCS from SOI substrate to a borofloat glass substrate [61, 142-144]. In short, after patterning the Si PCS membrane on the SOI substrate the sample is immersed into a hydrofluoric acid solution to etch the buried oxide. Once the sacrificial oxide layer is removed the suspended PCS is picked up with a PDMS stamp. The peeling back is done quickly to overcome the bonding forces between the PCS membrane and the donor substrate. On successful removal of the PCS membrane from the Si surface, it is applied onto a borofloat glass substrate. The PCS membrane bonds with the receiver substrate with a weak Van der Waal's force. To have a well printed sample the peeling speed during pick up should be fast while the peeling speed during release of the membrane should be slow. That is why this kind of printing is also known as kinetically controlled transfer printing. The glass with the transferred PCS is then attached to a microfluidic channel (width 500µm, length 900µm, and depth 120µm) fabricated on a silicon chip using deep reactive ion etching (DRIE) via anodic bonding. Figure 5-3 show the reflection spectra of the PCS after transfer on a glass substrate with a microscope image of the transferred PC. Small inherent angle in the incident beam makes the symmetry protected bound states in the continuum (BIC) mode B visible. Completion of the fabrication process is carried out by coating the PCS with a thin layer of polymer OV-101 through static coating process [145].

As the transferred Si structure on borofloat glass is coated with polymer, the spectral position of the resonance mode in the reflection spectrum experiences a red shift. The relationship between spectral shift and polymer thickness is simulated and shown in Figure 5-4(a). Design of the 2D PCS was done using Stanford Stratified Structure Solver (S^4) software package [146]. As the polymer thickness increases, the spectral shift

increases linearly initially and then gradually slows down until reaching a plateau around 300 nm. The slope of the resonance shift in relation to polymer thickness is 0.33 nm/nm for polymer thickness under 60 nm. The saturation in the spectral shift is caused by the near-zero mode distribution. Figure 5-4(b) presents the measured reflection spectrum of the PCS after the coating process. A red shift of 7.5 nm is presented by the resonance mode in the reflection spectra. This corresponds to a 20 nm polymer thickness according to the simulation result shown in Figure 5-4(a). After coating, the Q-factor of mode B degrades further to 9 K, which is expected due to nonuniformity and surface texture of the coating.

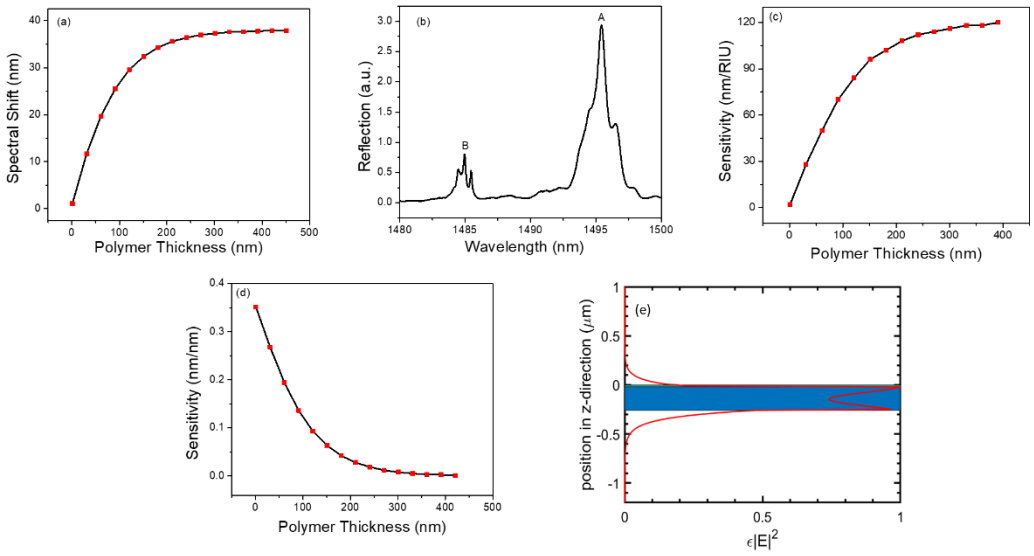

Figure 5-4 (a) Simulated spectral shift of PCS sensor for different polymer thicknesses (b) Measured reflection spectra of the transferred PCS sensor after coating (c) RI sensitivity for different polymer thickness (d) Thickness sensitivity for different polymer thickness (e) Distribution of integrated $\epsilon|E|^2$ in one unit cell along vertical (z-axis) direction for polymer thicknesses of 20 nm

On exposure to VOC molecules, the polymer layer on the PCS sensor swells up and experiences a change in the refractive index. This causes a spectral shift in the resonance of the PCS according to the relation below [147]:

$$\lambda = (\partial\lambda/\partial n).\Delta n + (\partial\lambda/\partial t).\Delta t \tag{5.1}$$

Here, n and t are refractive index and thickness of the polymer. $S_{RI} = \partial\,\lambda/\partial\,n$ and $S_t = \partial\,\lambda/\partial\,t$ represents the RI sensitivity and thickness sensitivity of the optical mode under investigation, respectively. The RI sensitivity for different polymer thickness is calculated and presented in Figure 5-4(c). S_{RI} is calculated by tracing the spectral shift in the reflection spectrum of the PCS for small changes in the refractive index of the polymer around 1.4. Increase in S_{RI} follows a linear relationship with rise in polymer thickness up to 100 nm then gradually saturates at 118 nm for polymer thicker than 300 nm. The thickness sensitivity is plotted in Figure 5-4(d). Reduction in the sensitivity of the optical mode is observed with increase in polymer thickness. As the polymer thickness approaches 300 nm the PCS sensor is hardly sensitive to change in polymer thickness. A metric of performance for any optical sensor in the sensitivity which can be derived from the optical overlap integral, f computed from this simulation. It can be defined as the ratio of the electric field energy in the polymer region to the total energy for a given mode [39, 148]:

$$f = \frac{\int_{V_{polymer}} \varepsilon|E|^2 dv}{\int_{V_{total}} \varepsilon|E|^2 dv} \tag{5.2}$$

Here ε is the dielectric constant of the material and E is the electric field. The higher the optical overlap integral the higher would be the RI sensitivity. Their relationship can be explained as $S_{RI} = \Delta\lambda/\Delta n = f.\lambda_0/n$ where λ_0 is the resonant wavelength and n is the polymer RI. Figure 5-4(e) displays the field energy, $\varepsilon|E|^2$ integrated along the z axis over one unit cell of the PCS for 20 nm of polymer on top. The simulation was done using finite-difference time-domain (FDTD) software package of MEEP [149]. Tracking further from the Si-polymer or Si-buried oxide interface shows exponential decaying of the field energy. The SRI for the PCS with a 20 nm polymer is calculated as 23.5 nm/RIU for a f of 1.58%.

5.3.2 Detection Limit Characterization

For vapor analysis it is very important to determine the limits of detection. Hence, detection limit for the PCS sensor is characterized in Table 5-2 for 10 VOCs. A tedlar bag containing either a high or low concentration sample of each analyte was connected to the μGC setup. Based on the sampling time and flow rate of the vacuum pump a fixed mass of the analyte gets accumulated in the dual adsorbent preconcentrator. All sampling times were kept less than 10 min and the sampling flow rate was 5 mL/min. The calibration curve for each of the 10 analytes is shown in Figure 5-5. Sampling mass of the individual analytes were varied over three orders of magnitude between 0-1500 ng. Each solid line in Figure 5-5 represents linear fitting of the 5-point raw data which was used to estimate the sensitivity of the analytes. Slope of the fitted line represents the analyte sensitivity in pm/ng. The sensitivity of the analytes is also outlined in Table 2. R^2 value for all the fitted lines were greater than 0.98. Linearity of the PCS spectral shift was also examined for the 10 VOCs. The response of the PCS sensor to all the analytes were

highly linear over 3 orders of magnitude sampling mass. As the sampling mass increases the spectral shift also increases linearly. Ethylbenzene and toluene exhibit the highest sensitivity while pentane shows the lowest. Since OV-101 is a non-polar polymer, it is supposed to interact with non-polar analytes like ethylbenzene and toluene more and have higher sensitivity. However, polarity is not the only factor that should be considered here. The fraction of the analyte that stays within the polymer in equilibrium with the carrier gas on top of it is also a determining factor. This fraction is determined by the partition coefficient of the polymer for a specific analyte as shown in Table 5-1. The higher the partition coefficient, the analyte tends to stay more in the polymer layer rather than the mobile phase. Pentane in this case has the lowest partition coefficient among the 10 analytes which causes it to have a lower sensitivity compared to the other analytes. Limit of detection for each of the VOC is calculated using:

$$DL = \frac{3\sigma}{S} \tag{5.3}$$

where, 3σ is the resolution of the spectral shift and S is the analyte sensitivity shown in Table 2. Detection limit of the PCS sensor for the 10 analytes range from 7 ng to 36 ng. Since limit of detection is inversely proportional to the sensitivity, the analytes with the highest sensitivity (toluene and ethylbenzene) demonstrate the lowest limit of detection 7.52 ng and 7.18 ng, respectively. The highest detection limit is for pentane amounting to 36.36 ng.

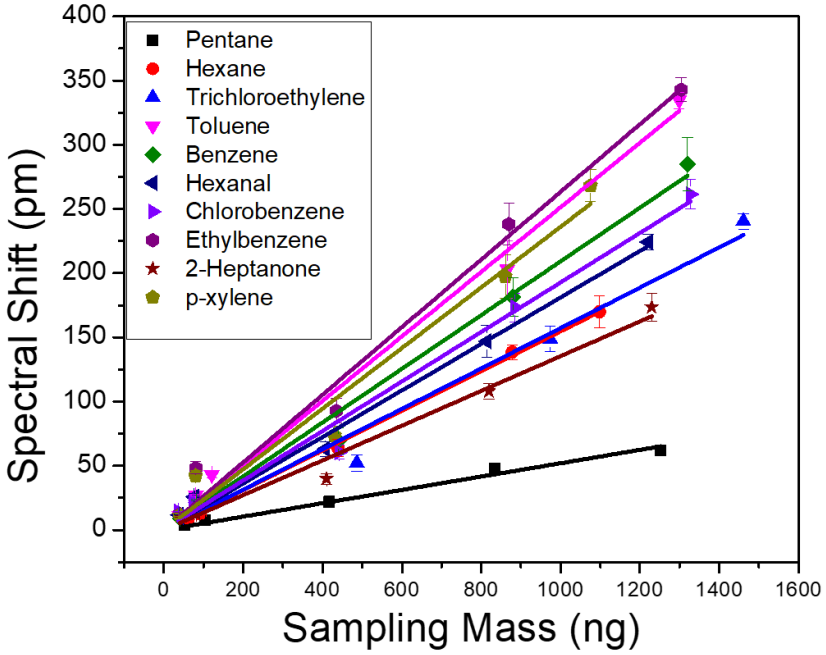

Figure 5-5 Spectral shift obtained as function of sampling mass on a linear scale for 10 VOCs. All analytes are separated with the same column temperature ramping at 1 mL/min.

Table 5-2 Sensitivity and detection limit characterization for a panel of 10 VOCs

Chemical Name	Sensitivity (pm/ng)	Standard Error	R^2	LOD (ng)
Pentane	0.05198	0.00189	0.99343	36.36
Hexane	0.15463	0.00182	0.99931	12.22
Benzene	0.20916	0.00768	0.9933	9.04
Trichloroethylene	0.15724	0.00757	0.98852	12.02
Toluene	0.25129	0.00702	0.99611	7.52
Hexanal	0.18107	0.0056	0.99524	10.44
Chlorobenzene	0.19274	0.00838	0.99062	9.81
Ethylbenzene	0.2633	0.01101	0.99132	7.18
p-xylene	0.23611	0.01369	0.98341	8.00
2- Heptanone	0.13536	0.0059	0.99057	13.96

5.3.3 Analyte Separation

To demonstrate the separation performance of the integrated μGC and PCS sensor system, in Figure 5-6(a) we put a mixture of 10 VOCs to test using a 10 m long

Rtx-5MS column. All the peaks are quite symmetric except 2- heptanone. Being a high boiling point analyte, it is most likely getting condensed in the stationary phase of the column as the column temperature is not high enough. However, this does not affect the overall resolution of the separation. Having very close boiling points and similar polarity, ethylbenzene (136 °C) and p-xylene (138 °C) are quite difficult to resolve [150-152]. They are both non-polar and have similar partition factor. As the peaks have sufficient separation, they can be identified in a mixture of analytes. Reduced temperature would have resolved them, but the analyzing time would be increased. Therefore, a trade-off between separation and overall analysis time is required. Rest of the analytes are well separated, and the test is completed within 4.2 min. The elution time could be further reduced using a higher flow rate or a shorter column at the expense of separation capacity. Details of the analyte mixture and their peak widths are detailed in Table 5-3. All injected mass were kept less than 500 ng and the peak width less than 5.1 s is achieved in all cases.

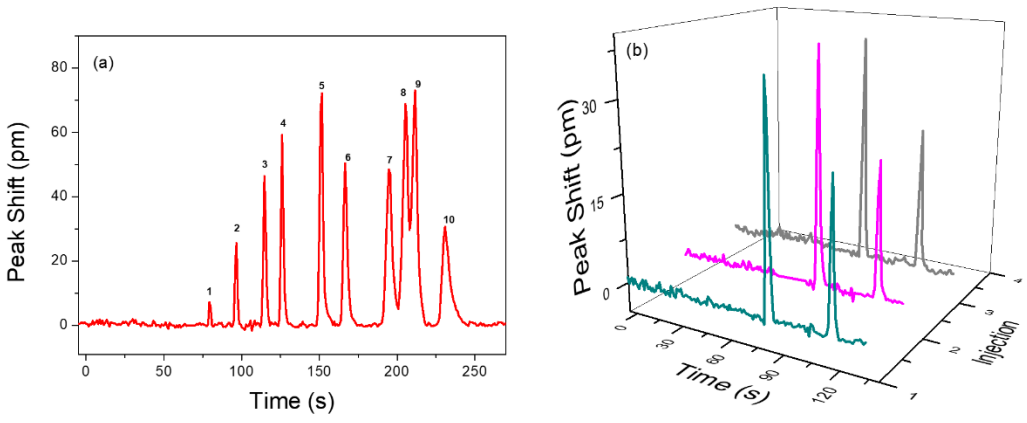

Figure 5-6 (a) Temperature programmed chromatogram for a VOC panel consisting of 10 VOC in a 10 m column with helium as carrier gas flowing at 1 mL/min. Details of the peaks are provided in Table 5-3 (b) Repeatability of peaks demonstrated with a mixture of benzene (82 ng) and

pentane (776 ng) flowing through the sensor under the same conditions over three consecutive injection.

Figure 5-6(b) describes the repeatability and reliability of analyte injection into the μGC system. A mixture of benzene and pentane in pumped into the μGC system over 3 consecutive injections. The retention time, peak width and spectral shift were reproduced with high precision. The standard deviation on the spectral shift of pentane and benzene is less than 4%.

Table 5-3 Details of VOC mixture separation in Figure 5-6

Peak #	Chemical	Sampling Mass (ng)	FWHM (s)	Peak Shift (pm)
1	Pentane	209	1.3	7.2
2	Hexane	220	1.8	25.6
3	Benzene	293	1.9	46.5
4	Trichloroethylene	488	1.8	59.3
5	Toluene	289	2.4	72.2
6	Hexanal	271	2.8	50.4
7	Chlorobenzene	369	4.1	48.5
8	Ethylbenzene	290	3.6	68.9
9	p-xylene	287	4.0	73.0
10	2-Heptanone	273	5.1	30.7

5.3.4 Analyte separation and detection with a PCS in microfabricated GC column

We also performed on-chip separation and detection by transferring the PCS sensor at the end of a microfabricated silicon column. An angled scanning electron micrograph (SEM) image of the column is presented in Figure 5-7(a). Figure 5-7(b) shows a 3 m microcolumn fabricated on silicon with DRIE and 5-7(c) illustrates the PCS sensor sitting at the outlet of the column. The on-chip column has a channel width of 250 μm and depth of 120 μm. After fabrication, the silicon column is anodically bonded to a borofloat glass, the bonded side of which houses the transferred PCS. Fused silica capillary glued to the ends of the silicon channel serves as inlet and outlet of the chip.

Subsequently, the column was coated with OV-101 polymer along with the PCS sensor. The column was characterized using a mixture of 4 analytes, hexane, heptane, benzene, and toluene. Flow rate for the carrier gas helium was set at 1 mL/min and the process was performed under isothermal conditions at room temperature. Analyte mass ranging from 200-300 ng was sampled within 4 min and the analysis was completed in another 2 minutes. So, the analysis was very rapid and did not consume any extra power for column heating. The peak width for the analytes varies from 3 to 5.5 s. Figure 5-7(d) shows the chromatogram for the on-column detection.

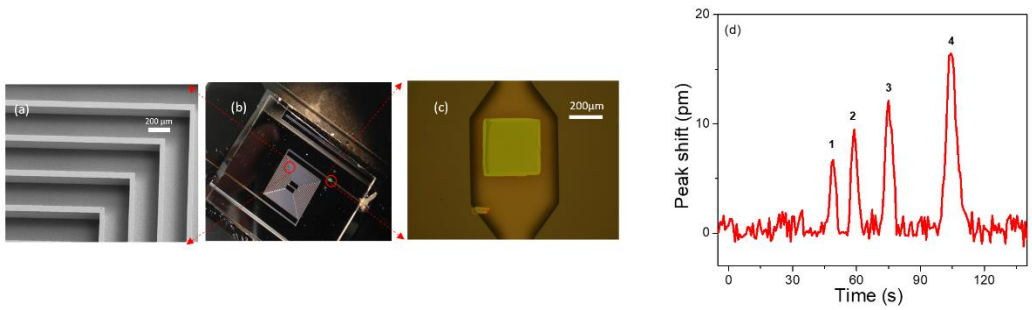

Figure 5-7 (a) Angled view SEM image of a Si column (b) An image of the Si column bonded with glass (c) Microscope image of the transferred PCS at the outlet of the column (d) Chromatogram for separation of hexane, heptane, benzene and toluene in a 3 m on chip silicon column with helium carrier gas at 1 mL/min at room temperature. Sampling mass and FWHM for the analytes are 1. Hexane (220 ng) (3.15 s), 2. Benzene (293 ng) (3.50 s), 3. Heptane (226 ng) (4.24 s) 4. Toluene (289 ng) (5.53 s).

5.4 Conclusions

We have developed a compact, non-destructive, fast and user-friendly vapor sensing system by integration of a free space coupled 2D PCS sensor with µGC. The defect free PCS sensor uses the shift in its intrinsic Fano resonance caused by adsorption of vapor molecules onto the sensing polymer to detect VOCS of different variety. Simulation results on RI and thickness sensitivity along with their electric field energy distribution of the PCS sensor has been reported. The PCS sensor's RI and thickness

sensitivity reached a standstill after 300 nm of polymer thickness. This trend was also confirmed by the electric field energy distribution. Spectral shift in the PCS sensor exhibited linear relationship with the concentration of the analyte. Detection limit obtained from the calibration curves of individual analyte were less then few tens of ng. Ethylbenzene shows the highest sensitivity while pentane shows the lowest. Factors like partition factor, polarity and vapor pressure must be considered to determine a chemical's sensitivity. The integrated system showed complete separation and detection for a complex mixture of 10 chemicals. Fast separation and detection were exhibited by on chip microfabricated column as well.

Chapter 6

Summary and Outlook

In this dissertation, we have successfully developed an integrated micro gas chromatography (µGC) system with 2D photonic crystal detector. The PC-µGC system has been characterized with 10 VOCs individually to achieve detection limit in order of few tens of ng. Additionally, we demonstrated complete separation of the 10 VOC mixture in 4.2 min. Performance of the PC sensor as a detector in an on-chip column was also explored. We also showed method development for analytes detection in gaseous samples which would ensure workplace safety and health monitoring. Being non-destructive, small, quick, and straightforward to use this system showed promising performance as a stand-alone vapor detection system.

Although this research has made significant progress towards it motive of creating an integrated and automated VOC analysis system that can accurately identify VOCs at low ppm to ppb level, there are still some limitations. The system is not yet completely portable. Even though, the cross-polarization optical setup required to obtain the reflection spectrum of the PC sensor is small and can be setup in any place on an optical board, it cannot be carried around as it is. This is because the alignment of optical components is crucial to getting a good signal response. So, the future steps of this project would include reduction of the incident light source and detection system to on-chip version for the PC sensor. We have used helium cartridges for the operation of the µGC system in this project. Use of ambient air as carrier gas could reduce the maintenance cost of the system and make the system adaptable for situation where a specific carrier gas might be expensive or difficult to acquire. This is also a feature that

we would like to explore next. The system uses electricity from standard electrical outlet and then converts it into specific DC voltage for different components of the μGC system. To make it suitable for situation where a power source might not be available, we also need to survey stored power or battery operation of the system. On column vapor separation at room temperature was reported in this project using an on-chip column with a PC sensor at the outlet of the column. Having an integrated heater on the backside of the chip would improve the separation performance and open possibility for a variety of applications. This feature would also be investigated subsequently.

References

1. Shimadzu Scientific Instruments. *What is Gas Chromatography?* 2021 [cited 2021; Available from: https://www.ssi.shimadzu.com/products/gas-chromatography/fundamental-guide-to-gas-chromatography/what-is-gas-chromatography.html.
2. Zhou, M., et al., *A fully automated portable gas chromatography system for sensitive and rapid quantification of volatile organic compounds in water.* RSC advances, 2016. **6**(55): p. 49416-49424.
3. Terry, S.C., J.H. Jerman, and J.B. Angell, *A gas chromatographic air analyzer fabricated on a silicon wafer.* IEEE transactions on electron devices, 1979. **26**(12): p. 1880-1886.
4. Yablonovitch, E., *Inhibited spontaneous emission in solid-state physics and electronics.* Physical review letters, 1987. **58**(20): p. 2059.
5. John, S., *Strong localization of photons in certain disordered dielectric superlattices.* Physical review letters, 1987. **58**(23): p. 2486.
6. Robinson, S. and R. Nakkeeran, *Photonic crystal ring resonator based optical filters.* Advances in Photonic Crystals, 2013. **1**: p. 1-26.
7. Bruyant, A., et al., *All-silicon omnidirectional mirrors based on one-dimensional photonic crystals.* Applied physics letters, 2003. **82**(19): p. 3227-3229.
8. Li, Y., et al., *Tunable terahertz-mirror and multi-channel terahertz-filter based on one-dimensional photonic crystals containing semiconductors.* Journal of Applied physics, 2011. **110**(7): p. 073111.
9. Chen, M.-C., P.-G. Luan, and C.-T. Lee. *Novel design of organic one-dimensional photonic crystal filter*. in *CLEO/Pacific Rim 2003. The 5th Pacific Rim Conference on Lasers and Electro-Optics (IEEE Cat. No. 03TH8671)*. 2003. IEEE.
10. Němec, H., et al., *Thermally tunable filter for terahertz range based on a one-dimensional photonic crystal with a defect.* Journal of applied physics, 2004. **96**(8): p. 4072-4075.
11. Lee, H.-Y., et al., *Multiple-wavelength-transmission filters based on Si-SiO 2 one-dimensional photonic crystals.* Journal of applied physics, 2005. **97**(10): p. 103111.
12. Taniyama, H., *Waveguide structures using one-dimensional photonic crystal.* Journal of applied physics, 2002. **91**(6): p. 3511-3515.
13. Lu, T.-W., et al., *One-dimensional photonic crystal nanobeam lasers on a flexible substrate.* Applied Physics Letters, 2011. **99**(7): p. 071101.
14. Rhouati, A., et al., *Label-Free Aptasensors for the Detection of Mycotoxins.* Sensors, 2016. **16**(12).

15. Crespi, A., et al., *Three-dimensional Mach-Zehnder interferometer in a microfluidic chip for spatially-resolved label-free detection.* Lab on a Chip, 2010. **10**(9): p. 1167-1173.
16. Zhang, T., et al., *A nanostructured Fabry-Perot interferometer.* Optics Express, 2010. **18**(19): p. 20282-20288.
17. Ymeti, A., et al., *Realization of a multichannel integrated Young interferometer chemical sensor.* Applied optics, 2003. **42**(28): p. 5649-5660.
18. Barrios, C.A., et al., *Label-free optical biosensing with slot-waveguides.* Optics letters, 2008. **33**(7): p. 708-710.
19. Homola, J., S.S. Yee, and G. Gauglitz, *Surface plasmon resonance sensors.* Sensors and actuators B: Chemical, 1999. **54**(1-2): p. 3-15.
20. Liedberg, B., C. Nylander, and I. Lunström, *Surface plasmon resonance for gas detection and biosensing.* Sensors and actuators, 1983. **4**: p. 299-304.
21. Matsubara, K., S. Kawata, and S. Minami, *Optical chemical sensor based on surface plasmon measurement.* Applied optics, 1988. **27**(6): p. 1160-1163.
22. Kruchinin, A. and Y.G. Vlasov, *Surface plasmon resonance monitoring by means of polarization state measurement in reflected light as the basis of a DNA-probe biosensor.* Sensors and Actuators B: Chemical, 1996. **30**(1): p. 77-80.
23. Mehan, N., et al., *Surface plasmon resonance based refractive index sensor for liquids.* 2005.
24. Shopova, S.I., et al., *On-Column Micro Gas Chromatography Detection with Capillary-Based Optical Ring Resonators.* Analytical Chemistry, 2008. **80**(6): p. 2232-2238.
25. Scholten, K., et al., *Nanoparticle-coated micro-optofluidic ring resonator as a detector for microscale gas chromatographic vapor analysis.* Nanoscale, 2015. **7**(20): p. 9282-9289.
26. Scholten, K., X. Fan, and E.T. Zellers, *A microfabricated optofluidic ring resonator for sensitive, high-speed detection of volatile organic compounds.* Lab Chip, 2014. **14**(19): p. 3873-80.
27. Yang, J.-C., et al., *Metallic nanohole arrays on fluoropolymer substrates as small label-free real-time bioprobes.* Nano letters, 2008. **8**(9): p. 2718-2724.
28. Fenzl, C., T. Hirsch, and O.S. Wolfbeis, *Photonic crystals for chemical sensing and biosensing.* Angewandte Chemie International Edition, 2014. **53**(13): p. 3318-3335.

29. Baker, J.E., R. Sriram, and B.L. Miller, *Two-dimensional photonic crystals for sensitive microscale chemical and biochemical sensing.* Lab on a Chip, 2015. **15**(4): p. 971-990.
30. Jorgenson, R.C. and S.S. Yee, *A fiber-optic chemical sensor based on surface plasmon resonance.* Sensors and Actuators B: Chemical, 1993. **12**(3): p. 213-220.
31. Xu, B., et al., *Hybrid Fabry-Perot interferometer for simultaneous liquid refractive index and temperature measurement.* Optics Express, 2017. **25**(13): p. 14483-14493.
32. Zheng, S., et al., *Sensitivity characterization of cladding modes in long-period gratings photonic crystal fiber for structural health monitoring.* Measurement, 2015. **72**: p. 43-51.
33. Liu, Y. and H.W.M. Salemink, *All-optical on-chip sensor for high refractive index sensing in photonic crystals.* EPL (Europhysics Letters), 2014. **107**(3): p. 34008.
34. Lai, W.-C., et al., *On-chip methane sensing by near-IR absorption signatures in a photonic crystal slot waveguide.* Optics Letters, 2011. **36**(6): p. 984-986.
35. Zhang, Y.-n., Y. Zhao, and Q. Wang, *Measurement of methane concentration with cryptophane E infiltrated photonic crystal microcavity.* Sensors and Actuators B: Chemical, 2015. **209**: p. 431-437.
36. Zhang, Y.-n., Y. Zhao, and Q. Wang, *Multi-component gas sensing based on slotted photonic crystal waveguide with liquid infiltration.* Sensors and Actuators B: Chemical, 2013. **184**: p. 179-188.
37. Liu, Y., et al., *Optofluidic vapor sensing with free-space coupled 2D photonic crystal slabs.* Scientific Reports, 2019. **9**(1): p. 4209.
38. Lai, W.-C., et al., *Multiplexed detection of xylene and trichloroethylene in water by photonic crystal absorption spectroscopy.* Optics Letters, 2013. **38**(19): p. 3799-3802.
39. Liu, Y., et al., *High quality factor photonic crystal filter at k ≈0 and its application for refractive index sensing.* Optics Express, 2017. **25**(9): p. 10536-10545.
40. Chang, Y.-H., Y.-Y. Jhu, and C.-J. Wu, *Temperature dependence of defect mode in a defective photonic crystal.* Optics Communications, 2012. **285**(6): p. 1501-1504.
41. Lu, T.-W. and P.-T. Lee, *Ultra-high sensitivity optical stress sensor based on double-layered photonic crystal microcavity.* Optics express, 2009. **17**(3): p. 1518-1526.
42. Casas-Bedoya, A., et al., *Chip scale humidity sensing based on a microfluidic infiltrated photonic crystal.* Applied Physics Letters, 2013. **103**(18): p. 181109.

43. Zheng, S., Y. Zhu, and S. Krishnaswamy, *Fiber humidity sensors with high sensitivity and selectivity based on interior nanofilm-coated photonic crystal fiber long-period gratings.* Sensors and Actuators B: Chemical, 2013. **176**: p. 264-274.
44. Kimble, K.W., et al., *Progress toward the development of a point-of-care photonic crystal ammonia sensor.* Analytical and bioanalytical chemistry, 2006. **385**(4): p. 678-685.
45. Alexeev, V.L., et al., *High ionic strength glucose-sensing photonic crystal.* Analytical chemistry, 2003. **75**(10): p. 2316-2323.
46. Shijie, Z., Z. Yinian, and K. Sridhar. *Nanofilm-coated photonic crystal fiber long-period gratings with modal transition for high chemical sensitivity and selectivity*. in *Proc.SPIE*. 2012.
47. Vuckovic, J., et al., *Optimization of the Q factor in photonic crystal microcavities.* IEEE Journal of Quantum Electronics, 2002. **38**(7): p. 850-856.
48. Coccioli, R., et al., *Smallest possible electromagnetic mode volume in a dielectric cavity.* IEE Proceedings-Optoelectronics, 1998. **145**(6): p. 391-397.
49. Qian, X., et al., *Theoretical research of gas sensing method based on photonic crystal cavity and fiber loop ring-down technique.* Sensors and Actuators B: Chemical, 2016. **228**: p. 665-672.
50. Li, K., et al., *$ L_ {n} $ Slot Photonic Crystal Microcavity for Refractive Index Gas Sensing.* IEEE Photonics Journal, 2014. **6**(5): p. 1-9.
51. Skivesen, N., et al., *Photonic-crystal waveguide biosensor.* Optics Express, 2007. **15**(6): p. 3169-3176.
52. Goyal, A.K. and S. Pal, *Design and simulation of high-sensitive gas sensor using a ring-shaped photonic crystal waveguide.* Physica Scripta, 2015. **90**(2): p. 025503.
53. Lin, C.-Y., et al., *Electro-optic polymer infiltrated silicon photonic crystal slot waveguide modulator with 23 dB slow light enhancement.* Applied Physics Letters, 2010. **97**(9): p. 194.
54. Lü, S., J. Zhao, and D. Zhang, *Flat band slow light in asymmetric photonic crystal waveguide based on microfluidic infiltration.* Applied optics, 2010. **49**(20): p. 3930-3934.
55. Kopp, C., et al., *Silicon photonic circuits: on-CMOS integration, fiber optical coupling, and packaging.* IEEE Journal of selected topics in quantum electronics, 2010. **17**(3): p. 498-509.
56. Xu, T., et al., *Pillar-array based optical sensor.* Optics Express, 2010. **18**(6): p. 5420-5425.

57. Goyal, A.K., H.S. Dutta, and S. Pal, *Recent advances and progress in photonic crystal-based gas sensors.* Journal of Physics D: Applied Physics, 2017. **50**(20): p. 203001.
58. Fano, U., *Effects of configuration interaction on intensities and phase shifts.* Physical Review, 1961. **124**(6): p. 1866.
59. Miroshnichenko, A.E., S. Flach, and Y.S. Kivshar, *Fano resonances in nanoscale structures.* Reviews of Modern Physics, 2010. **82**(3): p. 2257.
60. Luk'yanchuk, B., et al., *The Fano resonance in plasmonic nanostructures and metamaterials.* Nature materials, 2010. **9**(9): p. 707-715.
61. Zhou, W., et al., *Progress in 2D photonic crystal Fano resonance photonics.* Progress in Quantum Electronics, 2014. **38**(1): p. 1-74.
62. Nachef, K., et al., *Micro gas chromatography sample injector for the analysis of natural gas.* Journal of Microelectromechanical Systems, 2012. **21**(3): p. 730-738.
63. Segal, A., et al., *Development of membrane extraction with a sorbent interface–micro gas chromatography system for field analysis.* Journal of Chromatography A, 2000. **873**(1): p. 13-27.
64. Dziuban, J.A., et al., *Portable gas chromatograph with integrated components.* Sensors and Actuators A: Physical, 2004. **115**(2): p. 318-330.
65. Liu, J., et al., *Demonstration of motionless Knudsen pump based micro-gas chromatography featuring micro-fabricated columns and on-column detectors.* Lab on a Chip, 2011. **11**(20): p. 3487-3492.
66. Akbar, M., et al., *A purge and trap integrated microGC platform for chemical identification in aqueous samples.* Analyst, 2014. **139**(13): p. 3384-3392.
67. Qin, Y. and Y.B. Gianchandani, *A fully electronic microfabricated gas chromatograph with complementary capacitive detectors for indoor pollutants.* Microsystems & Nanoengineering, 2016. **2**(1): p. 15049.
68. Lu, H.-T., Y. Qin, and Y. Gianchandani, *A Microvalve Module with High Chemical Inertness and Embedded Flow Heating for Microscale Gas Chromatography.* Sensors, 2021. **21**(2).
69. Ricoul, F., et al., *Integrated System for the Rapid Polycyclic Aromatic Hydrocarbons Extraction from Aqueous Samples and Their Consecutive Thermal Desorption Prior to Gas Chromatography Analysis.* American Journal of Analytical Chemistry, 2020. **11**(2): p. 75-89.
70. Zampolli, S., et al., *Compact-GC platform: A flexible system integration strategy for a completely microsystems-based gas-chromatograph.* Sensors and Actuators B: Chemical, 2020. **305**: p. 127444.
71. Lu, C.-J. and E.T. Zellers, *A dual-adsorbent preconcentrator for a portable indoor-VOC microsensor system.* Analytical chemistry, 2001. **73**(14): p. 3449-3457.

72. Lu, C.J. and E.T. Zellers, *Multi-adsorbent preconcentration/focusing module for portable-GC/microsensor-array analysis of complex vapor mixtures.* Analyst, 2002. **127**(8): p. 1061-1068.
73. Namieśnik, J., *Preconcentration of gaseous organic pollutants in the atmosphere.* Talanta, 1988. **35**(7): p. 567-587.
74. Mitra, S. and C. Yun, *Continuous gas chromatographic monitoring of low concentration sample streams using an on-line microtrap.* Journal of Chromatography A, 1993. **648**(2): p. 415-421.
75. Peng, C.-Y. and S. Batterman, *Performance evaluation of a sorbent tube sampling method using short path thermal desorption for volatile organic compounds.* Journal of Environmental Monitoring, 2000. **2**(4): p. 313-324.
76. Wei-Cheng, T., et al., *Multiple-stage microfabricated preconcentrator-focuser for micro gas chromatography system.* Journal of Microelectromechanical Systems, 2005. **14**(3): p. 498-507.
77. Mohsen, Y., et al., *Selection and characterization of adsorbents for the analysis of an explosive-related molecule traces in the air.* Sensors and Actuators B: Chemical, 2013. **176**: p. 124-131.
78. Mohsen, Y., et al., *Development of a micro-analytical prototype for selective trace detection of orthonitrotoluene.* Microchemical Journal, 2014. **114**: p. 48-52.
79. Bang, J., et al., *A carbon nanotube sponge as an adsorbent for vapor preconcentration of aromatic volatile organic compounds.* Journal of Chromatography A, 2019. **1605**: p. 460363.
80. Lee, J. and S.-H. Lim, *CNT Foam-Embedded Micro Gas Preconcentrator for Low-Concentration Ethane Measurements.* Sensors, 2018. **18**(5).
81. Lee, J., J. Lee, and S.-H. Lim, *Micro gas preconcentrator using metal organic framework embedded metal foam for detection of low-concentration volatile organic compounds.* Journal of Hazardous Materials, 2020. **392**: p. 122145.
82. Garg, A., et al., *Zebra GC: A mini gas chromatography system for trace-level determination of hazardous air pollutants.* Sensors and Actuators B: Chemical, 2015. **212**: p. 145-154.
83. Bryant-Genevier, J. and E.T. Zellers, *Toward a microfabricated preconcentrator-focuser for a wearable micro-scale gas chromatograph.* J Chromatogr A, 2015. **1422**: p. 299-309.
84. Camara, M., et al., *Tubular gas preconcentrators based on inkjet printed micro-hotplates on foil.* Sensors and Actuators B: Chemical, 2016. **236**: p. 1111-1117.
85. Han, B., et al., *Micro-fabricated packed metal gas preconcentrator for enhanced monitoring of ultralow concentration of isoprene.* Journal of Chromatography A, 2018. **1572**: p. 27-36.

86. McCartney, M.M., et al., *An Easy to Manufacture Micro Gas Preconcentrator for Chemical Sensing Applications.* ACS Sensors, 2017. **2**(8): p. 1167-1174.
87. Radadia, A.D., et al., *The effect of microcolumn geometry on the performance of micro-gas chromatography columns for chip scale gas analyzers.* Sensors and Actuators B: Chemical, 2010. **150**(1): p. 456-464.
88. Akbar, M., H. Shakeel, and M. Agah, *GC-on-chip: integrated column and photoionization detector.* Lab on a Chip, 2015. **15**(7): p. 1748-1758.
89. Phyo, S., et al., *A 3D-printed metal column for micro gas chromatography.* Lab on a Chip, 2020. **20**(18): p. 3435-3444.
90. Regmi, B.P. and M. Agah, *Micro Gas Chromatography: An Overview of Critical Components and Their Integration.* Analytical Chemistry, 2018. **90**(22): p. 13133-13150.
91. Sun, J., et al., *Compact prototype GC-PID system integrated with micro PC and micro GC column.* Journal of Micromechanics and Microengineering, 2019. **29**(3): p. 035008.
92. Bulbul, A. and H. Kim, *A bubble-based microfluidic gas sensor for gas chromatographs.* Lab on a Chip, 2015. **15**(1): p. 94-104.
93. Tombez, L., et al., *Methane absorption spectroscopy on a silicon photonic chip.* Optica, 2017. **4**(11): p. 1322-1325.
94. Kuipers, W. and J. Müller, *Characterization of a microelectromechanical systems-based counter-current flame ionization detector.* Journal of Chromatography A, 2011. **1218**(14): p. 1891-1898.
95. Haghighi, F., Z. Talebpour, and A. Sanati-Nezhad, *Through the years with on-a-chip gas chromatography: a review.* Lab Chip, 2015. **15**(12): p. 2559-75.
96. Narayanan, S., B. Alfeeli, and M. Agah, *Two-Port Static Coated Micro Gas Chromatography Column With an Embedded Thermal Conductivity Detector.* IEEE Sensors Journal, 2012. **12**(6): p. 1893-1900.
97. Reddy, K., et al., *Rapid, sensitive, and multiplexed on-chip optical sensors for micro-gas chromatography.* Lab Chip, 2012. **12**(5): p. 901-5.
98. Chen, F.-Y., et al., *Novel gas chromatographic detector utilizing the localized surface plasmon resonance of a gold nanoparticle monolayer inside a glass capillary.* Analytical chemistry, 2014. **86**(11): p. 5257-5264.
99. Sun, Y., et al., *Rapid tandem-column micro-gas chromatography based on optofluidic ring resonators with multi-point on-column detection.* Analyst, 2010. **135**(1): p. 165-71.
100. Scholten, K., X. Fan, and E.T. Zellers, *A microfabricated optofluidic ring resonator for sensitive, high-speed detection of volatile organic compounds.* Lab on a Chip, 2014. **14**(19): p. 3873-3880.

101. Scholten, K., et al., *Nanoparticle-coated micro-optofluidic ring resonator as a detector for microscale gas chromatographic vapor analysis.* Nanoscale, 2015. **7**(20): p. 9282-9289.
102. Venkatasubramanian, A., et al., *Nano-Optomechanical Systems for Gas Chromatography.* Nano Lett, 2016. **16**(11): p. 6975-6981.
103. Zhu, H., et al., *Flow-through microfluidic photoionization detectors for rapid and highly sensitive vapor detection.* Lab on a Chip, 2015. **15**(14): p. 3021-3029.
104. Siegel, R.L., et al., *Cancer statistics, 2021.* CA: a cancer journal for clinicians, 2021. **71**(1): p. 7-33.
105. Pauling, L., et al., *Quantitative Analysis of Urine Vapor and Breath by Gas-Liquid Partition Chromatography.* Proceedings of the National Academy of Sciences of the United States of America, 1971. **68**(10): p. 2374-2376.
106. Phillips, M., et al., *Volatile organic compounds in breath as markers of lung cancer: a cross-sectional study.* The Lancet, 1999. **353**(9168): p. 1930-1933.
107. Chen, X., et al., *A study of the volatile organic compounds exhaled by lung cancer cells in vitro for breath diagnosis.* Cancer, 2007. **110**(4): p. 835-44.
108. Peng, G., E. Trock, and H. Haick, *Detecting Simulated Patterns of Lung Cancer Biomarkers by Random Network of Single-Walled Carbon Nanotubes Coated with Nonpolymeric Organic Materials.* Nano Letters, 2008. **8**(11): p. 3631-3635.
109. Di Natale, C., et al., *Lung cancer identification by the analysis of breath by means of an array of non-selective gas sensors.* Biosensors and Bioelectronics, 2003. **18**(10): p. 1209-1218.
110. Chen, X., et al., *A study of an electronic nose for detection of lung cancer based on a virtual SAW gas sensors array and imaging recognition method.* Measurement Science and Technology, 2005. **16**(8): p. 1535-1546.
111. Bajtarevic, A., et al., *Noninvasive detection of lung cancer by analysis of exhaled breath.* BMC Cancer, 2009. **9**(1): p. 348.
112. Oguma, T., et al., *Clinical contributions of exhaled volatile organic compounds in the diagnosis of lung cancer.* PLOS ONE, 2017. **12**: p. e0174802.
113. Yu, H., L. Xu, and P. Wang, *Solid phase microextraction for analysis of alkanes and aromatic hydrocarbons in human breath.* Journal of Chromatography B, 2005. **826**(1): p. 69-74.
114. Song, G., et al., *Quantitative breath analysis of volatile organic compounds of lung cancer patients.* Lung Cancer, 2010. **67**(2): p. 227-231.

115. Crohns, M., et al., *Exhaled pentane as a possible marker for survival and lipid peroxidation during radiotherapy for lung cancer—a pilot study.* Free Radical Research, 2009. **43**(10): p. 965-974.
116. Preti, G., et al., *Analysis of lung air from patients with bronchogenic carcinoma and controls using gas chromatography-mass spectrometry.* Journal of Chromatography B: Biomedical Sciences and Applications, 1988. **432**: p. 1-11.
117. Poli, D., et al., *Exhaled volatile organic compounds in patients with non-small cell lung cancer: cross sectional and nested short-term follow-up study.* Respiratory Research, 2005. **6**(1): p. 71.
118. Poli, D., et al., *Determination of aldehydes in exhaled breath of patients with lung cancer by means of on-fiber-derivatisation SPME–GC/MS.* Journal of Chromatography B, 2010. **878**(27): p. 2643-2651.
119. Buszewski, B., et al., *Investigation of lung cancer biomarkers by hyphenated separation techniques and chemometrics*, in *Clinical Chemistry and Laboratory Medicine*. 2012. p. 573.
120. Phillips, M., et al., *Detection of Lung Cancer With Volatile Markers in the Breatha.* Chest, 2003. **123**(6): p. 2115-2123.
121. de Lacy Costello, B., et al., *A review of the volatiles from the healthy human body.* J Breath Res, 2014. **8**(1): p. 014001.
122. Azzouz, I., F. Marty, and T. Bourouina. *Recent advances in micro-gas chromatography—The opportunities and the challenges*. in *2017 Symposium on Design, Test, Integration and Packaging of MEMS/MOEMS (DTIP)*. 2017. IEEE.
123. Azzouz, I., et al., *Review of stationary phases for microelectromechanical systems in gas chromatography: feasibility and separations.* Analytical and Bioanalytical Chemistry, 2014. **406**(4): p. 981-994.
124. Ghosh, A. and M.L. Lee, *Substrate Materials Used in Microchip Gas Chromatography.* Scientia Chromatographica, 2018. **10**(3).
125. Ghosh, A., et al., *Microchip gas chromatography columns, interfacing and performance.* Talanta, 2018. **188**: p. 463-492.
126. Moriaux, A.-L., et al., *Monitoring gas-phase CO2 in the headspace of champagne glasses through combined diode laser spectrometry and micro-gas chromatography analysis.* Food Chemistry, 2018. **264**: p. 255-262.
127. Zampolli, S., et al., *A MEMS-Enabled Deployable Trace Chemical Sensor Based on Fast Gas-Chromatography and Quartz Enhanced Photoacousic Spectoscopy.* Sensors, 2020. **20**(1).
128. Tung, B.T., et al., *Strain Sensitive Effect in a Triangular Lattice Photonic Crystal Hole-Modified Nanocavity.* IEEE Sensors Journal, 2011. **11**(11): p. 2657-2663.

129. Singh, S., R.K. Sinha, and R. Bhattacharyya, *Photonic crystal slab waveguide-based infiltrated liquid sensors: design and analysis.* Journal of Nanophotonics, 2011. **5**(1): p. 053505.
130. Zhang, Y.-n., Y. Zhao, and Q. Wang, *Optimizing the slow light properties of slotted photonic crystal waveguide and its application in a high-sensitivity gas sensing system.* Measurement Science and Technology, 2013. **24**(10): p. 105109.
131. Kumar, A., T.S. Saini, and R.K. Sinha, *Design and analysis of photonic crystal biperiodic waveguide structure based optofluidic-gas sensor.* Optik, 2015. **126**(24): p. 5172-5175.
132. Goyal, A.K., H.S. Dutta, and S. Pal, *Performance optimization of photonic crystal resonator based sensor.* Optical and Quantum Electronics, 2016. **48**(9): p. 1-11.
133. Sünner, T., et al., *Photonic crystal cavity based gas sensor.* Applied Physics Letters, 2008. **92**(26): p. 261112.
134. Isidorov, V.A. and V.T. Vinogorova, *Experimental determination and calculation of distribution coefficients between air and fiber with polydimethylsiloxane coating for some groups of organic compounds.* Journal of Chromatography A, 2005. **1077**(2): p. 195-201.
135. Kloskowski, A., et al., *Partition coefficients of selected environmentally important volatile organic compounds determined by gas–liquid chromatography with polydimethylsiloxane stationary phase.* The Journal of Chemical Thermodynamics, 2005. **37**(1): p. 21-29.
136. Bicchi, C., et al., *Headspace sorptive extraction (HSSE) in the headspace analysis of aromatic and medicinal plants.* Journal of High Resolution Chromatography, 2000. **23**(9): p. 539-546.
137. Avila, M.A.S. and R. Breiter, *Estimating the PDMS-coated, SPME-fibre/water-and fibre/gas-partition coefficients of chlorinated ethenes by headspace-SPME.* Chromatographia, 2007. **66**(5): p. 369-376.
138. Martos, P.A., A. Saraullo, and J. Pawliszyn, *Estimation of air/coating distribution coefficients for solid phase microextraction using retention indexes from linear temperature-programmed capillary gas chromatography. Application to the sampling and analysis of total petroleum hydrocarbons in air.* Analytical chemistry, 1997. **69**(3): p. 402-408.
139. Tian, W.-C., et al., *Multiple-stage microfabricated preconcentrator-focuser for micro gas chromatography system.* Journal of Microelectromechanical systems, 2005. **14**(3): p. 498-507.
140. Liu, Y., W. Zhou, and Y. Sun, *Optical Refractive Index Sensing Based on High-Q Bound States in the Continuum in Free-Space Coupled Photonic Crystal Slabs.* Sensors, 2017. **17**(8).

141. Shuai, Y., et al., *Coupled double-layer Fano resonance photonic crystal filters with lattice-displacement.* Applied Physics Letters, 2013. **103**(24): p. 241106.
142. Meitl, M.A., et al., *Transfer printing by kinetic control of adhesion to an elastomeric stamp.* Nature materials, 2006. **5**(1): p. 33-38.
143. Zhou, W., et al., *Flexible photonic-crystal Fano filters based on transferred semiconductor nanomembranes.* Journal of Physics D: Applied Physics, 2009. **42**(23): p. 234007.
144. Yang, H., et al. *Transfer printed nanomembranes for heterogeneously integrated membrane photonics*. in *Photonics*. 2015. Multidisciplinary Digital Publishing Institute.
145. Reidy, S., et al., *High-performance, static-coated silicon microfabricated columns for gas chromatography.* Analytical Chemistry, 2006. **78**(8): p. 2623-2630.
146. Liu, V. and S. Fan, *S4: A free electromagnetic solver for layered periodic structures.* Computer Physics Communications, 2012. **183**(10): p. 2233-2244.
147. Sun, Y. and X. Fan, *Analysis of ring resonators for chemical vapor sensor development.* Optics Express, 2008. **16**(14): p. 10254-10268.
148. El Beheiry, M., et al., *Sensitivity enhancement in photonic crystal slab biosensors.* Optics express, 2010. **18**(22): p. 22702-22714.
149. Oskooi, A.F., et al., *MEEP: A flexible free-software package for electromagnetic simulations by the FDTD method.* Computer Physics Communications, 2010. **181**(3): p. 687-702.
150. Walker, J. and D. Ahlberg, *Quantitative Analysis of Aromatic Hydrocarbons by Capillary Gas Chromatography.* Analytical Chemistry, 1963. **35**(13): p. 2022-2027.
151. Regulations, O., *Standard Test Method for Analysis of p-Xylene by Gas Chromatography.*
152. Frysinger, G.S., R.B. Gaines, and E.B. Ledford Jr, *Quantitative determination of BTEX and total aromatic compounds in gasoline by comprehensive two-dimensional gas chromatography (GC× GC).* Journal of High Resolution Chromatography, 1999. **22**(4): p. 195-200.

Biographical Information

Priyanka Biswas received her Bachelor of Science degree in Electrical, Electronics and Communication Engineering from Military Institute of Science and Technology in 2014. She started her PhD degree in Electrical Engineering at the University of Texas at Arlington in 2016. Her research has been focusing on the development of micro sensors for volatile organic compound sensing. She has successfully demonstrated integration of micro photoionization detector and photonic crystal slab sensor in micro gas chromatography. The system has potential application in environmental safety and disease diagnosis. Next, Ms. Biswas intends to pursue career in the field of integrated sensing and automated system development.